Available online at www.sciencedirect.com

ScienceDirect

European Journal of Mechanics / A Solids (2026) 1–54

European Journal of Mechanics / A Solids

Supplementary Information

Supplementary Information for: Symmetry breaking and emergent shear–normal coupling in two-point periodic lattices

Sondipon Adhikari[a,1,*]

[a]*James Watt School of Engineering, The University of Glasgow, Glasgow G12 8QQ, UK*

Abstract

This supplement collects the detailed derivations underlying the main text. It gives the full proofs of the symmetry and obstruction results and the complete energy-based derivation of the effective compliance of two-point Y-type hexagonal lattices, together with the parameter studies and the small-asymmetry analysis summarized in the main paper.

Three results are established. First (Theorem S7), a uniformly decorated admissible Y-type hexagonal lattice possesses the reflection symmetry $R : (x, y) \mapsto (-x, y)$ if and only if the two branches at a junction are images of one another under that reflection, a condition called branch balance; and branch balance is not a consequence of periodicity, since the closure identity of a hexagonal cell of this class holds for every choice of branch projections. Second (Theorem S3), the reflection symmetry forces the shear-normal compliances S_{13} and S_{23} to vanish, so a uniformly decorated and branch balanced lattice cannot exhibit coupling for any admissible geometry; a uniformly decorated lattice with unbalanced branches, obtained by slipping successive rows horizontally, is admissible and generically coupled (Proposition S2.8). Third (Theorem S1), two is the smallest basis supporting the alternating arrangement developed here, in which neighbouring junctions carry mirror-image decorations.

The derivation in Section S3 obtains the effective compliance directly from the strain energy of the two-point supercell under uniform macroscopic stress, giving closed-form expressions for all six coefficients in terms of the dimensionless geometric parameters. Evaluating these expressions over the design space shows that the two-point lattices span a wide range of Poisson's ratios while keeping the compliance matrix positive definite, and that the shear-normal coefficients change sign along identifiable curves in the parameter plane.

Taken with the main paper, these derivations show that the mirror content of the unit cell, to which the branch geometry at a single junction and the decoration of the periodic basis contribute jointly, governs which couplings a homogeneous Y-type lattice can express, with the cell geometry then setting their magnitude and sign.

Contents

*Corresponding author

Email address: Sondipon.Adhikari@glasgow.ac.uk (Sondipon Adhikari)

[1]Professor of Engineering Mechanics

Relation to the main paper

This document supports and extends the main paper. The main paper states the three results, the mirror criterion for uniformly decorated lattices together with the demonstration that branch balance is not forced by periodicity, the emergence of shear-normal coupling in two-point lattices, and the minimality of the two-point arrangement, and gives the reasoning in outline together with the closed-form coefficients and their design consequences. Here we supply the parts that the main text states without full derivation. Section S2 gives the complete proofs of the mirror criterion and of the constitutive consequence $S_{13} = S_{23} = 0$, together with the closure computation showing that the horizontal balance $a_L + a_R = 0$ is not implied by the periodicity of the cell. Section S3 carries out the energy-based homogenization in full: the supercell construction, the unique-ligament energy counting, the loading decompositions, and the extraction of every compliance coefficient, so that the closed-form expressions quoted in the main paper can be reproduced step by step. The remaining sections provide corroboration and detail that the main paper only summarizes: the exact recovery of the classical one-point honeycomb as a special case, the parameter studies of Section S5 mapping Poisson's ratios, positive-definiteness, and the sign-change curves of S_{13} and S_{23}, and the small-asymmetry expansion of Section S6 showing that the coupling grows linearly away from the symmetric limit. Section and equation numbers in this supplement are internal to this document; references to the main paper are named explicitly where they occur.

S1. Mathematical Framework and Definitions

This section establishes the mathematical foundation for our analysis of periodic lattice materials. We define the class of structures under consideration and establish the homogenization framework that relates microscale geometry to macroscale constitutive response. All definitions are accessible to readers familiar with linear elasticity without requiring advanced mathematical formalism.

S1.1. Periodic Lattice Structures

We formalize the notion of a periodic lattice as an embedded graph with translational symmetry.

Definition S1.1 (Bravais lattice)**.** A *Bravais lattice* in $\mathbb{R}^2$ is a discrete subgroup of the additive group $(\mathbb{R}^2, +)$, that is a set of the form

$$\Lambda = \{n_1\mathbf{a}_1 + n_2\mathbf{a}_2 : n_1, n_2 \in \mathbb{Z}\}, \tag{S1}$$

where $\mathbf{a}_1, \mathbf{a}_2 \in \mathbb{R}^2$ are linearly independent vectors called *lattice vectors* or *primitive translations*.

The lattice vectors span a two-dimensional lattice that tiles the plane. The *fundamental domain* (or primitive cell) is the parallelogram

$$\mathcal{F} = \{s_1\mathbf{a}_1 + s_2\mathbf{a}_2 : 0 \le s_1, s_2 < 1\}. \tag{S2}$$

Every point in $\mathbb{R}^2$ can be uniquely written as $\mathbf{r} + \boldsymbol{\lambda}$ where $\mathbf{r} \in \mathcal{F}$ and $\boldsymbol{\lambda} \in \Lambda$.

Definition S1.2 (Periodic embedded lattice)**.** A *periodic embedded lattice* is a structure $\mathcal{L}$ consisting of:

1. A countable set of vertices V representing junction points,
2. A set of edges E representing elastic beam members connecting vertices,
3. An embedding in $\mathbb{R}^2$ such that each vertex has a definite position and each edge is a straight line segment,
4. A Bravais lattice Λ such that the structure is invariant under translation by any $\boldsymbol{\lambda} \in \Lambda$: for every vertex at position $\mathbf{r}$, there exists a vertex at position $\mathbf{r} + \boldsymbol{\lambda}$ with identical local connectivity and geometry.

Remark S1.3. In the context of architected materials, vertices represent junction points where beam members meet, and edges represent elastic ligaments. The periodicity ensures that the structure can tile the plane indefinitely by repeating a finite motif.

Definition S1.4 (Junction type and basis size)**.** Let v be a vertex of a periodic embedded lattice with Bravais lattice Λ. The *junction data* of v is the set of edge vectors incident on v together with the material and cross-sectional properties carried by those edges. Let

$$\Gamma = \langle \Lambda, \rho \rangle, \qquad \rho : (x, y) \mapsto (-x, -y), \tag{S3}$$

be the group generated by the lattice translations together with the two-fold rotation ρ. Two vertices have the same *junction type* when their junction data agree after the action of an element of Γ, and the *basis size* n_{basis} is the number of junction types, that is the number of orbits of vertices under Γ. A lattice is called:

- *one-point* (or *monatomic*) if $n_{\text{basis}} = 1$,
- *two-point* (or *diatomic*) if $n_{\text{basis}} = 2$,
- *n-point* (or *n-atomic*) if $n_{\text{basis}} = n$.

We also call a one-point lattice *uniformly decorated*, since all its junctions carry the same geometric data.

Remark S1.5 (The two orientations of Y junction, and why the group is generated by ρ). A Y-hexagonal lattice always contains two orientations of junction: an upward Y whose stem points down and whose branches point up, and a downward Y whose stem points up

and whose branches point down. These two orientations are never related by a translation of Λ, so a definition of basis size that quotients by translations alone would assign basis size two to every lattice of the class, including the classical honeycomb in which both orientations carry identical data. The distinction on which this work rests would then be empty.

The two orientations are related by the two-fold rotation ρ about the midpoint of the stem joining them, and in the admissible class this relation is automatic: if the upward Y at the origin has edge vectors $(0, -h)$, (a_L, b_L) and (a_R, b_R), then the downward Y reached along either branch has edge vectors $(0, h)$, $(-a_L, -b_L)$ and $(-a_R, -b_R)$, which is precisely the ρ image. Quotienting by $\Gamma = \langle \Lambda, \rho \rangle$ therefore makes n_{basis} count inequivalent *decorations*, and the classical honeycomb is one-point as intended.

The use of ρ rather than a mirror is essential and not a matter of taste. A mirror such as $m : (x, y) \mapsto (x, -y)$ relates the two orientations equally well, but any lattice invariant under m has $C_{13} = C_{23} = 0$ by Theorem S3, since m acts on the strain vector through the same matrix $\mathrm{diag}(1, 1, -1)$ as the reflection R used there. Building a mirror into the definition of $n_{\text{basis}} = 1$ would therefore place the conclusion of Corollary S2.11 inside the definition, and the obstruction theory would be vacuous. The rotation ρ carries no such content: $\rho = -\mathbf{I}$ acts on second-order tensors with the factor $(-1)^2$ and on fourth-order tensors with $(-1)^4$, so it leaves every component of the planar elasticity tensor unconstrained. In crystallographic terms, n_{basis} counts decorated junctions inequivalent under Γ; it is not the number of sites in the primitive cell, which is two for any honeycomb.

Remark S1.6. The terminology "monatomic" and "diatomic" is borrowed from solid state physics, where it refers to crystal structures with one or two atoms per primitive cell. Here we apply the same concept to the junction points of elastic lattices.

Fig. S1 illustrates the basic distinction between one-point and two-point periodic lattices that underlies the present work. In both cases, the global structure is periodic and is generated by repeated translation of a fundamental domain $\mathcal{F}$ along the lattice vectors $\mathbf{a}_1$ and $\mathbf{a}_2$. The crucial difference lies not in the existence of periodicity itself, but in the number of geometrically distinct junctions contained within the periodic basis. In the one-point lattice shown in Fig. S1(a), every junction is equivalent under translation, so the lattice possesses a single junction type repeated throughout the plane. In the two-point lattice shown in Fig. S1(b), the basis contains two inequivalent junctions, denoted A and B, which are repeated periodically but are not mapped to one another by lattice translations alone. This enlargement of the basis is the key topological modification considered in this paper. It preserves the overall translational order of the lattice while allowing additional geometric asymmetry within each periodic repeat. As shown in the later sections, this distinction has constitutive consequences, although not in the unqualified form stated in the original version of this document. A uniformly decorated lattice whose two branches at a junction are images of one another under the reflection R carries that reflection symmetry and therefore has no shear–normal coupling; the two-point basis removes the uniformity and admits coupling, and it is the setting in which we obtain the complete closed-form compliance. Uniformity of the decoration is not by itself sufficient to exclude coupling, as Proposition S2.8 shows, and the precise statement is given in Theorem S7 and Corollary S2.11.

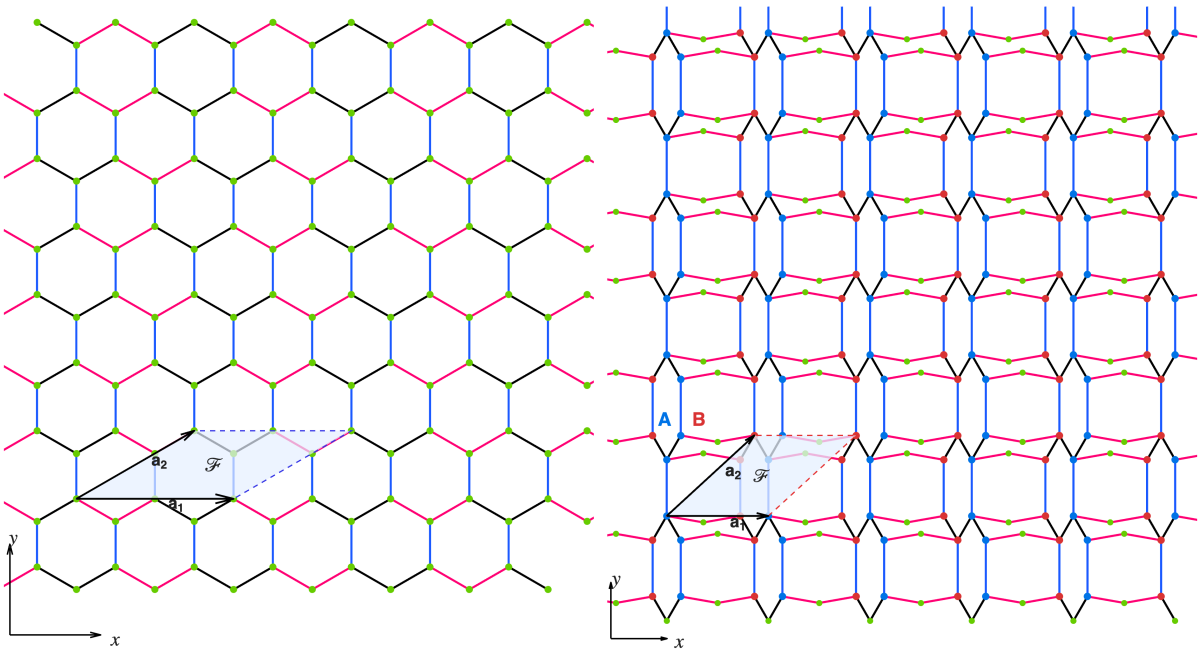

(a) One-point periodic lattice. (b) Two-point periodic lattice.

Fig. S1. Schematic representation of periodic lattice structures. In both panels, the lattice is generated by translating a fundamental domain $\mathcal{F}$ by integer combinations of the lattice vectors $\mathbf{a}_1$ and $\mathbf{a}_2$, which are indicated by arrows. The shaded parallelogram denotes one representative fundamental domain, and the coordinate axes (x, y) are shown for reference. In the one-point lattice, all junctions are geometrically identical and belong to a single equivalence class under lattice translations. In the two-point lattice, the periodic basis contains two inequivalent junction types, labeled A and B, which alternate throughout the structure. The two panels therefore illustrate how enlarging the basis from one point to two points preserves periodicity while introducing an additional internal degree of freedom at the unit-cell level.

S1.2. Y-Type Hexagonal Lattice Class

We now specialize to the class of planar lattices that is the focus of our analysis.

Definition S1.7 (Y-type junction)**.** A *Y-type junction* is a vertex of degree three in an embedded lattice graph, the *degree* of a vertex being the number of edges incident on it. The three incident edges are classified as:

- One *stem* edge, parallel to the y axis of the global Cartesian frame, which is the frame in which the compliance matrix is written,
- Two *branch* edges, whose inclinations are measured from the positive x direction and counted positive counterclockwise, and whose horizontal projections are nonzero and of opposite sign, so that one branch is left-inclined and the other right-inclined.

The name derives from the resemblance to the letter "Y".

Definition S1.8 (Admissible Y-type hexagonal lattice)**.** An *admissible Y-type hexagonal lattice* is a periodic embedded lattice satisfying:

1. Every vertex is a Y-type junction in the sense of Definition S1.7, with one stem parallel to the y axis of length $h > 0$ and two branches of nonzero horizontal projection and opposite sign,
2. The lattice tiles the plane with hexagonal cells, a *cell* being a bounded face of the embedded graph, that is a region enclosed by a circuit of members and containing

no member in its interior, and a cell being *hexagonal* when its boundary circuit has exactly six edges; the boundary circuit of each cell consists of four branches together with the two stems that link successive rows,

3. The basis size is finite: $n_{\text{basis}} \in \{1, 2, 3, \ldots\}$,
4. All beam members with the same geometric role have identical material and cross-sectional properties, where the *geometric role* of a member is the pair formed by its family, stem or left-inclined branch or right-inclined branch, and the junction type to which it belongs, so that a lattice of basis size n_{basis} carries at most $3n_{\text{basis}}$ roles,
5. Traversing the boundary circuit of a cell once, the six edges occur in the cyclic order branch, stem, branch, branch, stem, branch, so that the two stems are opposite edges of the hexagon and each branch family contributes two edges.

The requirement that all edges be embedded as straight segments is not repeated here, being already part of Definition S1.2. No metric regularity is implied by the word hexagonal: the six edges of a cell may have three distinct lengths and the interior angles need not be equal, and regular hexagons occur only in the special case $L_1 = L_2$, $\theta_1 = \theta_2 = 30^\circ$, $h = L_1$.

Remark S1.9. The hexagonal tiling condition ensures that the structure can support in-plane loads without gaps or overlaps when tessellated. The condition is combinatorial: it fixes the number of edges of a cell and the cyclic order in which the families appear around it, and it places no restriction on the metric regularity of the cell. The earlier phrase "near-hexagonal" has been removed, since it suggested a tolerance where none is needed; every cell of an admissible lattice is exactly hexagonal in the combinatorial sense, whatever its edge lengths and interior angles.

For this work, we focus on two principal cases:

- *Classical (one-point) Y-hexagonal lattices:* All Y-junctions in the lattice are geometrically identical up to translation. Each junction has one vertical member of length h and two inclined members of lengths L_1, L_2 at angles θ_1, θ_2. This is the standard configuration analyzed in classical lattice mechanics.
- *Two-point Y-hexagonal lattices:* The fundamental domain contains two geometrically distinct junction types, denoted A and B. Junctions of type A have their own characteristic geometric parameters $(h^A, L_1^A, L_2^A, \theta_1^A, \theta_2^A)$, while junctions of type B have parameters $(h^B, L_1^B, L_2^B, \theta_1^B, \theta_2^B)$. This enlarged basis is the central object of study in the present work.

Definition S1.10 (Geometric parameters)**.** For an admissible Y-type hexagonal lattice, the *geometric parameters* for each junction type $k = 1, \ldots, n_{\text{basis}}$ consist of:

- Vertical member length $h_k > 0$,
- Left branch member length $L_1^{(k)} > 0$ and angle $\theta_1^{(k)} \in (-\pi/2, \pi/2)$ measured from the positive x-axis,
- Right branch member length $L_2^{(k)} > 0$ and angle $\theta_2^{(k)} \in (-\pi/2, \pi/2)$.

All beam members have material properties (E, ν) and rectangular cross-section with thickness t and unit out-of-plane width, giving cross-sectional area $A = t$ and second moment of area $I = t^3/12$.

Definition S1.11 (Branch projections, branch balance and row slip)**.** For a junction with left branch (L_1, θ_1) and right branch (L_2, θ_2), write

$$a_L = -L_1 \cos\theta_1, \quad a_R = L_2 \cos\theta_2, \quad b_L = L_1 \sin\theta_1, \quad b_R = L_2 \sin\theta_2, \tag{S4}$$

so that the three edge vectors leaving the junction are $(0, -h)$ for the stem, (a_L, b_L) for the left branch and (a_R, b_R) for the right branch. The junction is *branch balanced* when

$$a_L + a_R = 0 \quad \text{and} \quad b_L = b_R, \tag{S5}$$

equivalently when $L_1 = L_2$ and $\theta_1 = \theta_2$, so that the two branches are images of one another under the reflection $R : (x, y) \mapsto (-x, y)$. The departure from balance is measured by the *row slip*

$$\delta_{\text{slip}} = \tfrac{1}{2}(a_L + a_R) = \tfrac{1}{2}\left(L_2 \cos\theta_2 - L_1 \cos\theta_1\right). \tag{S6}$$

Branch balance is a property of a single junction, whereas the basis size is a property of the arrangement of junctions. The two are logically independent, and both enter the obstruction theory of Section S2. This independence was not recognized in the original version of this document, in which balance was believed to follow from periodicity.

Throughout this work, we make the following simplifying assumptions:

- *Material homogeneity*: All beam members have the same Young's modulus E and Poisson's ratio ν.
- *Cross-section uniformity*: All members have rectangular cross-section with thickness t and unit out-of-plane width.
- *Euler-Bernoulli beam theory*: Each member behaves as a linear elastic beam with axial and bending deformations governed by classical beam theory.

Under these assumptions, the only sources of geometric variation are the lengths $(h_k, L_1^{(k)}, L_2^{(k)})$ and angles $(\theta_1^{(k)}, \theta_2^{(k)})$ assigned to different junction types. This restriction isolates the geometric mechanisms of symmetry breaking from material and fabrication complexity. Within the homogeneous class there are two such mechanisms, unbalancing the branches at a single junction type and enlarging the decoration of the basis, and they are treated separately below.

S1.3. Homogenized Constitutive Law

We now describe how the microstructure of the periodic lattice gives rise to a macroscopic (homogenized) constitutive law relating average stress and strain. The homogenization is performed over a representative volume element (RVE) corresponding to the fundamental domain of the lattice.

S1.3.1. Strain and Stress Measures

For a planar structure under small deformations, the strain field is characterized by the in-plane strain vector

$$\boldsymbol{\varepsilon} = \begin{bmatrix} \varepsilon_{11} \\ \varepsilon_{22} \\ \gamma_{12} \end{bmatrix} = \begin{bmatrix} \dfrac{\partial u}{\partial x} \\ \dfrac{\partial v}{\partial y} \\ \dfrac{\partial u}{\partial y} + \dfrac{\partial v}{\partial x} \end{bmatrix}, \tag{S7}$$

where $u(x, y)$ and $v(x, y)$ are the displacement components in the x and y directions, respectively. Here ε_{11} and ε_{22} are normal strains, while γ_{12} is the engineering shear strain (equal to twice the tensorial shear strain).

The corresponding stress components are arranged as

$$\boldsymbol{\sigma} = \begin{bmatrix} \sigma_{11} \\ \sigma_{22} \\ \tau_{12} \end{bmatrix}, \tag{S8}$$

where σ_{11}, σ_{22} are normal stresses and τ_{12} is the shear stress.

S1.3.2. Compliance and Stiffness Tensors

The homogenized constitutive law in the linear elastic regime is expressed in *compliance form* as

$$\boldsymbol{\varepsilon} = \mathbf{S}\boldsymbol{\sigma}, \tag{S9}$$

where the *compliance matrix* $\mathbf{S}$ is a 3×3 symmetric matrix:

$$\mathbf{S} = \begin{bmatrix} S_{11} & S_{12} & S_{13} \\ S_{12} & S_{22} & S_{23} \\ S_{13} & S_{23} & S_{33} \end{bmatrix}. \tag{S10}$$

By symmetry of the strain energy, $\mathbf{S}$ is symmetric: $S_{ij} = S_{ji}$. Therefore, there are six independent compliance coefficients.

The inverse relation, written in *stiffness form*, is

$$\boldsymbol{\sigma} = \mathbf{C}\boldsymbol{\varepsilon}, \tag{S11}$$

where $\mathbf{C} = \mathbf{S}^{-1}$ is the *stiffness matrix*:

$$\mathbf{C} = \begin{bmatrix} C_{11} & C_{12} & C_{13} \\ C_{12} & C_{22} & C_{23} \\ C_{13} & C_{23} & C_{33} \end{bmatrix}. \tag{S12}$$

S1.3.3. Physical Interpretation of Compliance Coefficients

The compliance matrix entries encode the complete mechanical response of the homogenized material, relating applied stresses to resulting strains. Each coefficient has a direct physical interpretation that can be understood by considering three fundamental loading scenarios. We examine the constitutive relation $\boldsymbol{\varepsilon} = \mathbf{S}\boldsymbol{\sigma}$ under three pure loading cases: uniaxial stress in the 1-direction, uniaxial stress in the 2-direction, and pure shear.

Case 1: Uniaxial loading in 1-direction ($\sigma_{11} \neq 0$, $\sigma_{22} = \tau_{12} = 0$). When only σ_{11} is applied, the constitutive law yields three strain components:

$$\varepsilon_{11} = S_{11}\sigma_{11}, \tag{S13}$$

$$\varepsilon_{22} = S_{12}\sigma_{11}, \tag{S14}$$

$$\gamma_{12} = S_{13}\sigma_{11}. \tag{S15}$$

Case 2: Uniaxial loading in 2-direction ($\sigma_{22} \neq 0$, $\sigma_{11} = \tau_{12} = 0$). When only σ_{22} is applied, the strain components become:

$$\varepsilon_{11} = S_{12}\sigma_{22}, \tag{S16}$$

$$\varepsilon_{22} = S_{22}\sigma_{22}, \tag{S17}$$

$$\gamma_{12} = S_{23}\sigma_{22}. \tag{S18}$$

Case 3: Pure shear loading ($\tau_{12} \neq 0$, $\sigma_{11} = \sigma_{22} = 0$). When only shear stress is applied, the induced strains are:

$$\varepsilon_{11} = S_{13}\tau_{12}, \tag{S19}$$

$$\varepsilon_{22} = S_{23}\tau_{12}, \tag{S20}$$

$$\gamma_{12} = S_{33}\tau_{12}. \tag{S21}$$

We now interpret each of the six independent compliance coefficients based on these loading scenarios.

Direct compliance S_{11}. From equation (S13), the coefficient S_{11} quantifies the extensional strain induced by longitudinal stress: $\varepsilon_{11} = S_{11}\sigma_{11}$. This is the direct compliance in the 1-direction and equals the reciprocal of the equivalent Young's modulus: $S_{11} = 1/E_1^{\text{eq}}$. A compliant material (low stiffness) has large S_{11}, while a stiff material has small S_{11}.

Direct compliance S_{22}. From equation (S17), the coefficient S_{22} quantifies the transverse extensional response: $\varepsilon_{22} = S_{22}\sigma_{22}$. This is the direct compliance in the 2-direction and equals the reciprocal of the transverse Young's modulus: $S_{22} = 1/E_2^{\text{eq}}$. For lattices with directional anisotropy, S_{11} and S_{22} generally differ.

Shear compliance S_{33}. From equation (S21), the coefficient S_{33} relates pure shear stress to shear strain: $\gamma_{12} = S_{33}\tau_{12}$. This is the reciprocal of the equivalent shear modulus: $S_{33} = 1/G_{12}^{\text{eq}}$. Shear compliance characterizes the material's resistance to in-plane distortion without change in area.

Poisson coupling S_{12}. From equation (S14), when longitudinal stress σ_{11} is applied, the induced transverse strain is $\varepsilon_{22} = S_{12}\sigma_{11}$. Similarly, from equation (S16), transverse stress σ_{22} induces longitudinal strain $\varepsilon_{11} = S_{12}\sigma_{22}$. This coefficient characterizes Poisson coupling: the material's tendency to contract (or expand) laterally when stretched (or compressed) longitudinally. The equivalent Poisson's ratio is $\nu_{12}^{\text{eq}} = -S_{12}/S_{11}$, with the reciprocity relation $\nu_{12}/E_1 = \nu_{21}/E_2$ ensuring thermodynamic consistency. For typical materials, $S_{12} < 0$ (negative Poisson coupling), indicating lateral contraction under tension.

Shear-normal coupling S_{13}. From equation (S19), when pure shear stress τ_{12} is applied, the induced normal strain in the 1-direction is $\varepsilon_{11} = S_{13}\tau_{12}$. Conversely, from equation (S15), longitudinal stress σ_{11} induces shear strain $\gamma_{12} = S_{13}\sigma_{11}$. This coefficient quantifies an unusual constitutive response: the coupling between shear stress and normal strain in the 1-direction. A positive value $S_{13} > 0$ indicates that positive shear induces tensile strain (elongation) horizontally, while negative $S_{13} < 0$ indicates compressive strain (contraction). For isotropic materials, and for orthotropic materials whose symmetry axes align with the coordinate frame, $S_{13} = 0$; a nonzero S_{13} means the homogenized response is fully anisotropic in the chosen frame, lacking an axis-aligned reflection symmetry.

Shear-normal coupling S_{23}. From equation (S20), when pure shear stress τ_{12} is applied, the induced normal strain in the 2-direction is $\varepsilon_{22} = S_{23}\tau_{12}$. Similarly, from equation (S18), transverse stress σ_{22} induces shear strain $\gamma_{12} = S_{23}\sigma_{22}$. This coefficient quantifies the coupling between shear stress and normal strain in the 2-direction. The sign of S_{23} controls whether shear induces vertical extension (if $S_{23} > 0$) or vertical contraction (if $S_{23} < 0$). Like S_{13}, this coefficient vanishes for isotropic media and for orthotropic media with axis-aligned symmetry, and is nonzero only when the homogenized response is fully anisotropic in the chosen frame.

The coefficients S_{13} and S_{23} are of particular significance for this work. Nonzero shear-normal coupling occurs only when the material microstructure lacks certain reflection symmetries. The central result of this work is a precise characterization of that requirement: for Y-type hexagonal lattices, a uniformly decorated basis whose junctions are branch balanced enforces $S_{13} = S_{23} = 0$ through the resulting reflection symmetry, and both conditions are needed, since a uniformly decorated lattice with unbalanced branches is admissible and generically coupled. A two-point basis removes the uniformity

and generically permits $S_{13}, S_{23} \neq 0$.

S1.3.4. Strain Energy Density

The elastic strain energy density stored in the homogenized medium is a quadratic form in the strain:

$$W(\boldsymbol{\varepsilon}) = \frac{1}{2}\boldsymbol{\varepsilon}^T \mathbf{C}\boldsymbol{\varepsilon} = \frac{1}{2}\boldsymbol{\sigma}^T \mathbf{S}\boldsymbol{\sigma}. \tag{S22}$$

Expanding in components:

$$W = \frac{1}{2}\big(C_{11}\varepsilon_{11}^2 + C_{22}\varepsilon_{22}^2 + C_{33}\gamma_{12}^2 + 2C_{12}\varepsilon_{11}\varepsilon_{22} + 2C_{13}\varepsilon_{11}\gamma_{12} + 2C_{23}\varepsilon_{22}\gamma_{12}\big). \tag{S23}$$

The cross-terms $C_{13}\varepsilon_{11}\gamma_{12}$ and $C_{23}\varepsilon_{22}\gamma_{12}$ represent coupling between normal and shear deformations in the energy. The presence (or absence) of these terms is the energy-theoretic signature of shear-normal coupling. From the variational principle $\boldsymbol{\sigma} = \partial W/\partial\boldsymbol{\varepsilon}$, it follows that $\sigma_{11} = C_{11}\varepsilon_{11} + C_{12}\varepsilon_{22} + C_{13}\gamma_{12}$, which shows explicitly that $C_{13} \neq 0$ implies that shear strain γ_{12} contributes to normal stress σ_{11}. By the inverse relation (S9), this is equivalent to $S_{13} \neq 0$ implying that shear stress τ_{12} induces normal strain ε_{11}.

S1.3.5. Complementary Energy Form

The strain energy density above is written in terms of the stiffness matrix $\mathbf{C}$ and the strain vector. The same content is carried by the complementary energy density, and that is the form in which the coefficients of interest appear directly:

$$W^*(\boldsymbol{\sigma}) = \tfrac{1}{2}\boldsymbol{\sigma}^T \mathbf{S}\boldsymbol{\sigma} = \tfrac{1}{2}\left(S_{11}\sigma_{11}^2 + S_{22}\sigma_{22}^2 + S_{33}\tau_{12}^2 + 2S_{12}\sigma_{11}\sigma_{22} + 2S_{13}\sigma_{11}\tau_{12} + 2S_{23}\sigma_{22}\tau_{12}\right), \tag{S24}$$

with $\boldsymbol{\varepsilon} = \partial W^*/\partial\boldsymbol{\sigma}$ recovering (S9). The homogenization carried out in this document prescribes uniform macroscopic stress on the unit cell and evaluates the stored energy, so W^* is the natural potential for the calculation: the coefficients S_{13} and S_{23} are read off as those of $\sigma_{11}\tau_{12}$ and $\sigma_{22}\tau_{12}$, with no matrix inversion required, and this is how the closed forms of Section S3 are obtained. The stiffness form is retained alongside it because the symmetry argument of Theorem S3 is most transparent in terms of strain, which transforms directly under the reflection; the two forms are equivalent, since $\mathbf{C} = \mathbf{S}^{-1}$ and $W^*(\boldsymbol{\sigma}) = W(\boldsymbol{\varepsilon})$ at corresponding states.

This completes the mathematical framework. In the following sections, we will use these definitions to establish the criterion that characterizes when S_{13} and S_{23} must vanish, in terms of the mirror content of the unit cell.

S2. Obstruction Theory: One-Point Basis Cannot Generate Coupling

This section establishes the central mathematical result of our work in its corrected form: a periodic Y-type hexagonal lattice excludes shear-normal coupling exactly when its unit cell carries a mirror aligned with the coordinate axes, and that mirror requires two independent geometric ingredients. The argument proceeds in three stages. First, we show that reflection symmetry in the microstructure forces the coupling coefficients S_{13} and S_{23} to vanish, an algebraic consequence of material frame indifference. Second, we prove that a uniformly decorated admissible lattice possesses that reflection symmetry *if and only if* its junctions are branch balanced in the sense of Definition S1.11. Third, we show

that branch balance is not a consequence of periodicity, by computing the closure identity of the correct hexagonal cell and by exhibiting an admissible uniformly decorated lattice that violates balance and is generically coupled. The resulting statement, Corollary S2.11, therefore carries both hypotheses explicitly. The original version of this document asserted that the one-point basis alone forces the reflection symmetry, deriving that conclusion from the closure of a cell bounded by six inclined members. No cell of the class has that boundary when $h > 0$, and the corrected computation yields an identity rather than a constraint; the present section replaces the argument accordingly.

S2.1. Algebraic Obstruction: Symmetry Kills Coupling

We begin with a purely algebraic result that applies to any elastic medium with a particular geometric symmetry.

Definition S2.1 (Reflection symmetry)**.** A planar structure is said to possess *reflection symmetry about the y-axis* if its geometric configuration is invariant under the transformation

$$R : \mathbb{R}^2 \to \mathbb{R}^2, \quad R(x, y) = (-x, y). \tag{S25}$$

More precisely, a periodic lattice possesses reflection symmetry if the positions and connectivity of all junctions are preserved (up to lattice translations) when the coordinate x is replaced by $-x$.

Under the reflection R, the infinitesimal strain components transform according to the coordinate change rules:

Lemma S2.2 (Strain transformation under reflection)**.** *Under the reflection $R : (x, y) \mapsto (-x, y)$, the strain components transform as:*

$$\varepsilon_{11} \mapsto \varepsilon_{11}, \tag{S26}$$

$$\varepsilon_{22} \mapsto \varepsilon_{22}, \tag{S27}$$

$$\gamma_{12} \mapsto -\gamma_{12}. \tag{S28}$$

In matrix form, this is represented by the orthogonal transformation

$$\mathbf{Q} = \begin{bmatrix} 1 & 0 & 0 \\ 0 & 1 & 0 \\ 0 & 0 & -1 \end{bmatrix}. \tag{S29}$$

Proof. The strain components are defined as:

$$\varepsilon_{11} = \frac{\partial u}{\partial x}, \quad \varepsilon_{22} = \frac{\partial v}{\partial y}, \quad \gamma_{12} = \frac{\partial u}{\partial y} + \frac{\partial v}{\partial x}. \tag{S30}$$

Under reflection, if $(x, y) \to (-x, y)$ and we have displacement field (u, v), then for the material to be symmetric, we require $u(-x, y) = -u(x, y)$ (odd in x) and $v(-x, y) = v(x, y)$ (even in x). Then:

$$\varepsilon_{11} = \frac{\partial u}{\partial x}\Big|_{(x,y)} \to \frac{\partial}{\partial x'}[u(x', y)]_{x'=-x} = -\frac{\partial u}{\partial x}\Big|_{(-x,y)} = -\left(-\frac{\partial u}{\partial x}\right)\Big|_{(x,y)} = \varepsilon_{11}, \tag{S31}$$

$$\varepsilon_{22} = \frac{\partial v}{\partial y} \to \frac{\partial v}{\partial y} = \varepsilon_{22}, \tag{S32}$$

$$\gamma_{12} = \frac{\partial u}{\partial y} + \frac{\partial v}{\partial x} \to \frac{\partial}{\partial y}[-u] + \frac{\partial}{\partial x'}[v]_{x'=-x} = -\frac{\partial u}{\partial y} - \frac{\partial v}{\partial x} = -\gamma_{12}. \tag{S33}$$

This confirms (S26)–(S28). □

We can now state and prove the main algebraic obstruction theorem.

Theorem S3 (Reflection symmetry obstruction)**.** *Let $\mathcal{L}$ be a planar periodic elastic lattice with homogenized compliance matrix $\mathbf{S}$. If $\mathcal{L}$ possesses reflection symmetry $R : (x, y) \mapsto (-x, y)$ as in Definition S2.1, then the shear-normal coupling coefficients vanish:*

$$S_{13} = S_{23} = 0. \tag{S34}$$

Proof. The proof proceeds through four steps: (1) establish material frame indifference, (2) derive the symmetry constraint on the stiffness matrix, (3) show that this forces the off-diagonal coupling terms to vanish, and (4) transfer this result to the compliance matrix.

Step 1: Material frame indifference. The strain energy density $W(\boldsymbol{\varepsilon})$ must be invariant under the reflection symmetry. This is a consequence of the fact that the microstructure looks identical when viewed in the reflected coordinate system. Mathematically:

$$W(\boldsymbol{\varepsilon}) = W(\mathbf{Q}\boldsymbol{\varepsilon}) \quad \text{for all } \boldsymbol{\varepsilon} \in \mathbb{R}^3, \tag{S35}$$

where $\mathbf{Q}$ is the strain transformation matrix from Lemma S2.2.

Step 2: Symmetry constraint on stiffness. Using the quadratic form (S22), we have $W(\boldsymbol{\varepsilon}) = \frac{1}{2}\boldsymbol{\varepsilon}^T\mathbf{C}\boldsymbol{\varepsilon}$. The invariance condition (S35) becomes

$$\boldsymbol{\varepsilon}^T\mathbf{C}\boldsymbol{\varepsilon} = (\mathbf{Q}\boldsymbol{\varepsilon})^T\mathbf{C}(\mathbf{Q}\boldsymbol{\varepsilon}) = \boldsymbol{\varepsilon}^T\mathbf{Q}^T\mathbf{C}\mathbf{Q}\boldsymbol{\varepsilon}. \tag{S36}$$

Since this must hold for all $\boldsymbol{\varepsilon}$, we conclude

$$\mathbf{C} = \mathbf{Q}^T\mathbf{C}\mathbf{Q}. \tag{S37}$$

Step 3: Explicit calculation. Let us write the stiffness matrix explicitly:

$$\mathbf{C} = \begin{bmatrix} C_{11} & C_{12} & C_{13} \\ C_{12} & C_{22} & C_{23} \\ C_{13} & C_{23} & C_{33} \end{bmatrix}. \tag{S38}$$

We compute $\mathbf{Q}^T\mathbf{C}\mathbf{Q}$ step by step. First,

$$\mathbf{C}\mathbf{Q} = \begin{bmatrix} C_{11} & C_{12} & C_{13} \\ C_{12} & C_{22} & C_{23} \\ C_{13} & C_{23} & C_{33} \end{bmatrix} \begin{bmatrix} 1 & 0 & 0 \\ 0 & 1 & 0 \\ 0 & 0 & -1 \end{bmatrix} = \begin{bmatrix} C_{11} & C_{12} & -C_{13} \\ C_{12} & C_{22} & -C_{23} \\ C_{13} & C_{23} & -C_{33} \end{bmatrix}. \tag{S39}$$

Then,

$$\mathbf{Q}^T\mathbf{C}\mathbf{Q} = \begin{bmatrix} 1 & 0 & 0 \\ 0 & 1 & 0 \\ 0 & 0 & -1 \end{bmatrix} \begin{bmatrix} C_{11} & C_{12} & -C_{13} \\ C_{12} & C_{22} & -C_{23} \\ C_{13} & C_{23} & -C_{33} \end{bmatrix} = \begin{bmatrix} C_{11} & C_{12} & -C_{13} \\ C_{12} & C_{22} & -C_{23} \\ -C_{13} & -C_{23} & C_{33} \end{bmatrix}. \tag{S40}$$

Equating this with $\mathbf{C}$ from constraint (S37), we obtain:

$$C_{11} = C_{11} \quad \checkmark, \tag{S41}$$
$$C_{12} = C_{12} \quad \checkmark, \tag{S42}$$
$$C_{22} = C_{22} \quad \checkmark, \tag{S43}$$
$$C_{33} = C_{33} \quad \checkmark, \tag{S44}$$
$$C_{13} = -C_{13} \quad \Rightarrow \quad C_{13} = 0, \tag{S45}$$
$$C_{23} = -C_{23} \quad \Rightarrow \quad C_{23} = 0. \tag{S46}$$

Step 4: Transfer to compliance. With $C_{13} = C_{23} = 0$, the stiffness matrix has block-diagonal structure:

$$\mathbf{C} = \begin{bmatrix} C_{11} & C_{12} & 0 \\ C_{12} & C_{22} & 0 \\ 0 & 0 & C_{33} \end{bmatrix} = \begin{bmatrix} \mathbf{C}_{2\times 2} & \mathbf{0} \\ \mathbf{0}^T & C_{33} \end{bmatrix}. \tag{S47}$$

The inverse $\mathbf{S} = \mathbf{C}^{-1}$ of a block-diagonal matrix is also block-diagonal:

$$\mathbf{S} = \begin{bmatrix} \mathbf{S}_{2\times 2} & \mathbf{0} \\ \mathbf{0}^T & S_{33} \end{bmatrix}, \tag{S48}$$

where $\mathbf{S}_{2\times 2} = \mathbf{C}_{2\times 2}^{-1}$ and $S_{33} = 1/C_{33}$.

Therefore, $S_{13} = S_{23} = 0$, completing the proof. □

Remark S2.4 (Physical interpretation). Theorem S3 has a direct physical interpretation. Under reflection symmetry, normal strains ε_{11} and ε_{22} are unchanged (they are even functions of x), while shear strain γ_{12} changes sign (odd function of x). If coupling existed, i.e., if $S_{13} \neq 0$, then applying a shear stress τ_{12} would induce normal strain $\varepsilon_{11} = S_{13}\tau_{12}$. But under reflection, $\tau_{12} \mapsto -\tau_{12}$ (shear stress is odd), so we would have $\varepsilon_{11} \mapsto -S_{13}\tau_{12}$. For the material to be reflection-symmetric, we must have $\varepsilon_{11} \mapsto \varepsilon_{11}$, which forces $S_{13} = 0$. The same argument applies to S_{23}.

Remark S2.5 (Generality of result). Theorem S3 is completely general: it applies to any planar elastic medium (not just lattices) with the specified reflection symmetry. This is a standard result in continuum mechanics and materials science. The non-trivial aspect of our work lies in identifying exactly which geometric feature of a uniformly decorated Y-type hexagonal lattice this reflection symmetry is equivalent to, which we establish in the next subsection, and in showing that the feature in question is not supplied by periodicity.

S2.2. Geometric Criterion: Reflection Symmetry Holds Exactly When the Branches Balance

We now give the geometric half of the argument. The result is an equivalence rather than an implication, which is what makes it useful: it identifies the single geometric feature to which the reflection symmetry of a uniformly decorated cell is equivalent, and therefore identifies exactly what must be broken in order to obtain coupling.

Lemma S2.6 (Structure of one-point lattice)**.** *For an admissible one-point Y-type hexagonal lattice, there exists exactly one junction type in the sense of Definition S1.4. All Y-junctions of the lattice are related by elements of* $\Gamma = \langle \Lambda, \rho \rangle$ *and carry identical junction data: one stem parallel to* y *of length* h*, one left-inclined branch with edge vector*

(a_L, b_L) and one right-inclined branch with edge vector (a_R, b_R), where $a_L < 0 < a_R$. No relation between a_L and a_R is implied.

Proof. By Definition S1.4 a one-point basis means one orbit of vertices under Γ, and by Definition S1.7 each vertex has degree three with one stem and two branches of opposite horizontal projection. Junctions in the same Γ orbit have the same junction data up to a translation and possibly the rotation ρ, and by Remark S1.5 the rotation accounts exactly for the two orientations of Y. The final sentence records that the definition constrains the two branches only through the sign of their horizontal projections; the original version of this lemma asserted a "symmetric arrangement" of the two branches, which is the conclusion of Theorem S7 under an additional hypothesis and cannot be part of this lemma. □

Theorem S7 (Mirror criterion)**.** *Let $\mathcal{L}$ be an admissible Y-type hexagonal lattice with uniform decoration, $n_{basis} = 1$, whose junction type carries the edge vectors $(0, -h)$, (a_L, b_L) and (a_R, b_R) with $a_L < 0 < a_R$. Then $\mathcal{L}$ is invariant under the reflection $R : (x, y) \mapsto (-x, y)$ up to lattice translation if and only if the junction is branch balanced,*

$$a_L + a_R = 0 \quad \textit{and} \quad b_L = b_R. \tag{S49}$$

Proof. Sufficiency. Assume (S49) and set $a := -a_L = a_R > 0$ and $b := b_L = b_R$. The three edge vectors are $(0, -h)$, $(-a, b)$ and (a, b). Under R the stem maps to itself and the two branches interchange, so the junction data are preserved as a set. Following a branch and then a stem returns a junction of the same orientation, so the translation group of the lattice is

$$\Lambda = \langle (a_L,\, b_L + h),\ (a_R,\, b_R + h) \rangle = \langle (-a,\, b + h),\ (a,\, b + h) \rangle\,, \tag{S50}$$

and R exchanges the two generators, hence maps Λ onto itself. Since $n_{\text{basis}} = 1$, every junction is the image of the representative one under an element of Γ, and R commutes with ρ, so R carries $\mathcal{L}$ onto itself up to a translation in Λ. The decoration is preserved because condition (iv) of Definition S1.8 assigns identical properties to all members of a family and R exchanges the two branch families as wholes.

Necessity. Assume R leaves $\mathcal{L}$ invariant up to translation. Applying R to the junction data gives the set $\{(0, -h),\ (-a_L, b_L),\ (-a_R, b_R)\}$, which by invariance must be the junction data of some junction of $\mathcal{L}$, hence, by uniformity of the decoration, must coincide with $\{(0, -h),\ (a_L, b_L),\ (a_R, b_R)\}$. The stem is the only edge with zero horizontal projection and is fixed by R, so the two branches must be matched to one another. Since $a_L < 0 < a_R$, the reflection carries the left branch into the right half plane and conversely, so the only available matching is $(-a_L, b_L) = (a_R, b_R)$ together with $(-a_R, b_R) = (a_L, b_L)$. Either equality yields $a_R = -a_L$ and $b_R = b_L$, which is (S49). □

S2.3. Branch Balance Is Not Forced by Periodicity

The original version of this document derived $a_L + a_R = 0$ from the closure of a hexagonal cell, using the edge list

$$\mathbf{e}_0 = (a_R, b), \quad \mathbf{e}_1 = (a_L, b), \quad \mathbf{e}_2 = (a_R, b), \quad \mathbf{e}_3 = (a_L, -b), \quad \mathbf{e}_4 = (a_R, -b), \quad \mathbf{e}_5 = (a_L, -b), \tag{S51}$$

whose horizontal components sum to $3(a_L + a_R)$. That edge list describes a circuit of six oblique branches, three from each family, and no cell of the class has such a boundary

when $h > 0$: by conditions (ii) and (v) of Definition S1.8 the boundary of a cell contains the two stems that link successive rows. A hexagonal cell bounded by branches alone would require the stems to have zero length, which is excluded by condition (i).

Carrying the computation out on the correct cell gives no constraint. Traverse the boundary of one cell once, starting at a junction whose stem points away from the cell. By condition (v) the six edges appear in the cyclic order branch, stem, branch, branch, stem, branch, and opposite sides of the hexagon are parallel and are traversed in opposite senses, so each family contributes one forward and one reversed edge. The six edge vectors are

$$\mathbf{e}_0 = (a_R, b_R), \quad \mathbf{e}_1 = (0, h), \quad \mathbf{e}_2 = (a_L, b_L), \quad \mathbf{e}_3 = (-a_R, -b_R), \quad \mathbf{e}_4 = (0, -h), \quad \mathbf{e}_5 = (-a_L, -b_L), \tag{S52}$$

and their sum is

$$\sum_{i=0}^{5} \mathbf{e}_i = (a_R - a_R + a_L - a_L,\ b_R - b_R + b_L - b_L + h - h) = (0, 0), \tag{S53}$$

an identity in a_L, a_R, b_L, b_R and h. Closure is automatic, because every edge direction of the cell occurs once in each sense around the circuit and a telescoping sum of that form vanishes whatever the edge vectors are. No information about the horizontal projections can be extracted from it.

Proposition S2.8 (Slipped one-point lattice)**.** *Fix $h > 0$, $b > 0$, $a > 0$ and δ_{slip} with $|\delta_{slip}| < a$, and let the single junction type carry the edge vectors*

$$(0, -h), \qquad (a_L, b_L) = (\delta_{slip} - a,\ b)\,, \qquad (a_R, b_R) = (\delta_{slip} + a,\ b)\,. \tag{S54}$$

Translating this junction by the group (S50) *and inserting the stems and branches produces an admissible Y-type hexagonal lattice with $n_{basis} = 1$ for every value of δ_{slip}. The lattice is the balanced case $\delta_{slip} = 0$ with each successive pair of rows displaced horizontally by δ_{slip}, whence the name row slip. For $\delta_{slip} \neq 0$ the lattice is not invariant under R, its only point symmetry is the two-fold rotation ρ, which places no restriction on the planar elasticity tensor, and consequently S_{13} and S_{23} are not required to vanish and do not vanish for generic parameter values.*

Proof. Condition (i) of Definition S1.8 holds because the stem is parallel to y and the horizontal projections $\delta_{\text{slip}} \mp a$ are nonzero and of opposite sign, by $|\delta_{\text{slip}}| < a$. For condition (ii), the junctions at $(a_L, b + h)$ and $(a_R, b + h)$ are translates of the one at the origin and are therefore junctions of the same orientation; the left branch of the second and the right branch of the first both terminate at $(a_L + a_R,\ 2b + h)$, so the circuit

$$(0,0) \to (a_R, b) \to (a_R, b+h) \to (a_L + a_R,\ 2b+h) \to (a_L, b+h) \to (a_L, b) \to (0,0) \tag{S55}$$

closes, consists of six edges, encloses no member, and realizes the cyclic order required by condition (v). Condition (iii) is immediate and condition (iv) holds because a single junction type carries three geometric roles. That $n_{\text{basis}} = 1$ follows from Remark S1.5: the junctions whose stems point downward form the translation group Λ and those whose stems point upward are their images under ρ, so all junctions lie in a single orbit of Γ. Failure of R invariance for $\delta_{\text{slip}} \neq 0$ is Theorem S7, since $a_L + a_R = 2\delta_{\text{slip}} \neq 0$ even though $b_L = b_R$. Finally $\rho = -\mathbf{I}$ acts on second-order tensors with the factor $(-1)^2$ and on fourth-order tensors with $(-1)^4$, so it constrains no component of the elasticity tensor

and cannot force $S_{13} = S_{23} = 0$. □

Remark S2.9 (Why the earlier balance argument failed). The ingredients invoked in the original argument were a single junction type, hexagonal tiling and degree-three connectivity. The first two do constrain the lattice, but not in the horizontal direction: the tiling condition enters only through the closure identity (S53), which is a telescoping sum over a circuit in which each edge direction occurs once in each sense, and such a sum vanishes identically. Extracting a constraint on the horizontal projections would require a circuit in which one branch family appears with a net multiplicity, which a hexagonal cell of this class does not provide. The edge list (S51) does have that property, and this is precisely why it appeared to yield a constraint; it is not, however, the boundary of any cell of the lattice. Branch balance is therefore an extra hypothesis about the embedding and not a consequence of the combinatorics.

Remark S2.10 (On the vertical projections). The original version of this document contained a remark asserting that the closure condition also forces $b_L = b_R$, through the relation $3(a_R, b_R) + 3(a_L, b_L) = (0, 0)$, and then observed that its vertical part $b_L + b_R = 0$ is unsatisfiable for positive rises, before appealing to a different interpretation of closure. That remark is withdrawn. The relation it used is the one belonging to the incorrect edge list (S51), and the correct closure identity (S53) constrains neither $a_L + a_R$ nor $b_L - b_R$. The equality of the two rises is part of the balance condition (S49) and, like the horizontal part, has to be assumed rather than derived. The slipped lattice of Proposition S2.8 keeps $b_L = b_R$ and violates only the horizontal part, which is enough to remove the mirror; a construction violating only the vertical part is equally admissible.

S2.4. Main Obstruction Theorem

We can now state and prove the central result of this section by combining the algebraic and geometric theorems.

Corollary S2.11 (One-point obstruction under branch balance)**.** *Every admissible Y-type hexagonal lattice that is uniformly decorated,* $n_{basis} = 1$, and *branch balanced in the sense of Definition S1.11 satisfies*

$$S_{13} = S_{23} = 0. \tag{S56}$$

Neither hypothesis may be dropped. Uniform decoration without balance is realized by the slipped lattice of Proposition S2.8, which is generically coupled; balance at each junction without uniformity is not sufficient either, since the two-point construction of Section S3 is generically coupled.

Proof. By Theorem S7, a uniformly decorated admissible lattice whose junctions are branch balanced is invariant under $R : (x, y) \mapsto (-x, y)$ up to lattice translation. By Theorem S3, any planar elastic structure with that invariance has $S_{13} = S_{23} = 0$ in its homogenized compliance matrix. The two statements combine to give (S56). The counterexamples asserted in the final sentence are Proposition S2.8 and Corollary S3.4. □

Remark S2.12 (Which part of the argument is standard and which is not). Theorem S3 is algebraic: it follows from material frame indifference, applies to any structure with an axis-aligned mirror whatever its internal microstructure, and is standard. Theorem S7 is geometric, and its content is an equivalence between the mirror symmetry of a uniformly

decorated cell and the balance of its two branches. The contribution of this section lies in that equivalence together with the negative result of Section S2.3: balance is not implied by periodicity, because the closure identity of the correct cell is an identity. Corollary S2.11 therefore converts a question about the constitutive tensor into a question about one scalar, the row slip (S6), and about the decoration of the basis, without requiring knowledge of the specific geometric parameters $(h, L_1, L_2, \theta_1, \theta_2)$ or material properties (E, ν, t). We no longer describe the result as tying basis size to constitutive constraints, since basis size alone does not determine the mirror content of the cell.

Remark S2.13 (Direction of the implications). Writing (B) for branch balance and (U) for uniform decoration,

$$\text{(B) and (U)} \iff R\text{-invariance} \implies S_{13} = S_{23} = 0, \tag{S57}$$

where the left equivalence is Theorem S7 and the right implication is Theorem S3. The right implication is not reversible: a lattice may have vanishing coupling for reasons unrelated to an axis-aligned mirror, and two-point lattices with $L_1 = L_2$ and $\theta_1 = \theta_2$ are trivial examples, since they reduce to the balanced one-point case. The conjunction on the left is not implied by $n_{\text{basis}} = 1$ alone, which is the content of Proposition S2.8. The earlier version of this remark asserted that one-point basis is sufficient for vanishing coupling; that assertion is false as stated and is corrected here.

Remark S2.14 (Range of validity within the class). Within the balanced and uniformly decorated subclass the vanishing of the coupling coefficients is universal: regardless of the geometric parameters $(h, L_1, L_2, \theta_1, \theta_2)$, the material properties (E, ν) or the cross-sectional dimensions (t, I), every such configuration has $S_{13} = S_{23} = 0$, and no optimization inside that subclass can overcome it. The restriction follows from the mirror symmetry of the cell rather than from the basis size, and the two ways of removing that symmetry within the homogeneous setting are exactly the failure of balance and the failure of uniformity.

Remark S2.15 (Scope: material homogeneity assumption). The obstruction result in Corollary S2.11 assumes material homogeneity: all beam members share the same Young's modulus E, Poisson's ratio ν, and thickness t. If this assumption is relaxed—for example, if the vertical member has material properties (E_v, ν_v, t_v) distinct from the inclined members' properties (E_i, ν_i, t_i)—then material heterogeneity breaks the reflection symmetry of the *mechanical response* even when the geometric configuration possesses reflection symmetry. In this case, the compliance matrix may exhibit nonzero coupling coefficients $S_{13}, S_{23} \neq 0$ even in a one-point lattice.

This provides an alternative mechanism for achieving coupling through *material design* rather than topological enlargement. However, material heterogeneity introduces additional design variables (multiple sets of material properties) and may complicate fabrication, particularly for additive manufacturing, where multi-material printing remains challenging. The two-point approach developed in Section 4 achieves coupling through pure geometry with homogeneous materials, requiring the discrete change $n_{\text{basis}} = 1 \to 2$ followed by continuous geometric parameter optimization. This work treats that mechanism within the homogeneous material class. It is one of two geometric mechanisms, the other being the row slip of Proposition S2.8, and the design variable that controls the accessible constitutive space is the mirror content of the cell rather than the basis size on its own.

The geometric approach also has a conceptual advantage: it makes clear that coupling is a consequence of symmetry breaking at the unit cell level, reachable through material heterogeneity, through branch imbalance, or through enlargement of the basis. The two-point framework isolates the third of these and supplies its complete closed-form constitutive description.

S2.5. Summary of Obstruction Theory

We summarize the logical structure of the corrected obstruction theory in the following diagram:

Uniform Decoration and Branch Balance $n_{\text{basis}} = 1$ and $a_L + a_R = 0,\ b_L = b_R$
$\Updownarrow$ *(Theorem S7, an equivalence)*
Reflection Symmetry $R : (x, y) \mapsto (-x, y)$ is a symmetry of the embedded lattice
$\Downarrow$ *(Theorem S3)*
Vanishing Coupling Coefficients $S_{13} = S_{23} = 0$

The first relation is an equivalence, and this is the point at which the present version differs from the original, which asserted a downward implication from $n_{\text{basis}} = 1$ alone. The second implication is a standard consequence of material frame indifference. Read together they show that the accessible constitutive behavior is governed by the mirror content of the cell, to which both the branch geometry at a single junction and the decoration of the basis contribute.

This completes the obstruction theory. Two routes out of the uncoupled class follow immediately, and they are independent: unbalancing the branches at a single junction type, which is Proposition S2.8, and enlarging the basis to two points, which is the subject of the next section and the route for which we obtain the complete closed-form compliance.

S3. Two-Point Basis: Symmetry Breaking and Coupling Emergence

Having established that uniform decoration together with branch balance forces $S_{13} = S_{23} = 0$, and that neither condition follows from periodicity alone, we now demonstrate that removing uniformity by enlarging the basis to two points admits generic nonzero coupling coefficients. This section proceeds in three stages. First, we define the two-point unit cell geometry and introduce dimensionless parameters. Second, we prove that inequivalent geometric data at the two basis points generically break reflection symmetry. Third, we derive closed-form analytical expressions for all equivalent elastic properties, including the coupling coefficients S_{13} and S_{23}, using energy-based homogenization via Castigliano's theorem.

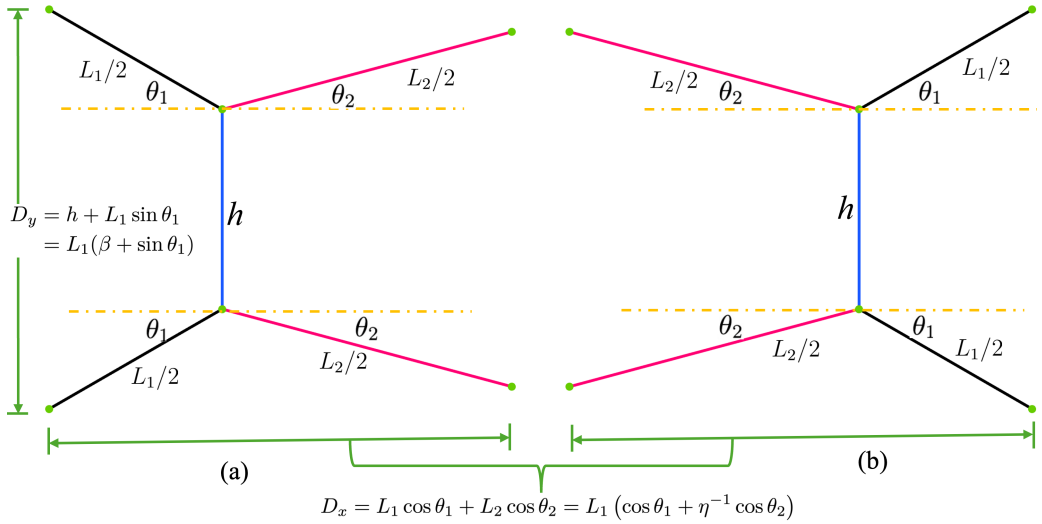

Fig. S2. Two-point unit cell construction with geometric parameters and projected dimensions. *(a)* Cell A: a vertical ligament of length h (blue) connected to two inclined half-members, with the left branch of length $L_1/2$ at angle θ_1 (black) and the right branch of length $L_2/2$ at angle θ_2 (pink/magenta). *(b)* Cell B: the complementary configuration where the positions of the L_1 and L_2 inclined members are interchanged. The dashed horizontal lines (orange) indicate the reference orientation for defining the inclination angles θ_1 and θ_2 measured from the horizontal. Green arrows indicate the projected supercell dimensions: vertical span $D_y = h + L_1\sin\theta_1 = L_1(\beta + \sin\theta_1)$ and horizontal span $D_x = L_1\cos\theta_1 + L_2\cos\theta_2 = L_1(\cos\theta_1 + \eta^{-1}\cos\theta_2)$, where $\eta = L_1/L_2$ and $\beta = h/L_1$ are the dimensionless length ratio and aspect ratio parameters. Junction points are marked by green dots. The pair (A,B) forms the minimal basis required to break reflection symmetry in the lattice. When $\eta \neq 1$ or $\theta_1 \neq \theta_2$, the asymmetry between cells A and B enables nonzero shear–normal coupling coefficients S_{13} and S_{23}.

S3.1. Two-Point Unit Cell Geometry

The fundamental building block of the proposed architecture is a two-point unit cell consisting of a pair of complementary Y-type junctions, denoted as cells A and B (see Figure S2).

Each cell comprises a vertical ligament of length h connected to two inclined members, but with distinct geometric properties: the black members have total parent length L_1 and angle θ_1, while the pink members have total parent length L_2 and angle θ_2. Crucially, each inclined member appears as a *half-member* in the unit cell description to avoid double-counting when the supercell is tessellated.

In contrast to classical single-point unit cells, where all junctions are identical and related by lattice translations, the present construction introduces two inequivalent junctions within a single periodic repeat. This enlargement of the basis from one point to two points fundamentally alters the symmetry of the lattice. In particular, the reflection symmetry present in the balanced single-point hexagonal lattice is removed, since cells A and B are not carried onto themselves by an axis-aligned mirror when $L_1 \neq L_2$ or $\theta_1 \neq \theta_2$. The two-point lattice therefore admits constitutive coupling effects, such as nonzero shear-normal coupling coefficients, that are excluded in the balanced and uniformly decorated case of Corollary S2.11. Two is the smallest basis supporting the alternating arrangement used here; it is not the smallest structure admitting coupling, since the slipped lattice of Proposition S2.8 couples with a single junction type.

S3.1.1. Geometric Parameters and Material Properties

The geometry of the two-point unit cell is characterized by the following parameters:

- h: vertical member length (common to both cells A and B),
- L_1: total parent length of black inclined members (appears as half-members $L_1/2$ in each cell),
- L_2: total parent length of pink inclined members (appears as half-members $L_2/2$ in each cell),
- θ_1: inclination angle of black members measured from horizontal,
- θ_2: inclination angle of pink members measured from horizontal.

For simplicity, we assume throughout this document that all members are made of the same material and have the same cross-sectional dimensions:

$$E_{\text{black}} = E_{\text{pink}} = E_{\text{vertical}} = E, \quad A = t, \quad I = \frac{t^3}{12}, \tag{S58}$$

where t is the member thickness and unit out-of-plane width is assumed. This assumption isolates the effect of geometric asymmetry from material heterogeneity.

S3.1.2. Dimensionless Parameters

To facilitate analysis and reveal the underlying scaling laws, we introduce three fundamental dimensionless parameters:

$$\eta = \frac{L_1}{L_2}, \quad \alpha = \frac{t}{L_1}, \quad \beta = \frac{h}{L_1}. \tag{S59}$$

Their physical interpretations are:

- η: *length ratio*, measuring the geometric disparity between the two inclined ligament families. When $\eta = 1$, both families have equal length. When $\eta \neq 1$, this introduces asymmetry.
- α: *slenderness parameter*, the ratio of thickness to black ligament length. Small α corresponds to slender beams where bending dominates; large α corresponds to stocky members where axial deformation becomes important.
- β: *normalized vertical height*, the ratio of vertical member length to black ligament length. This controls the aspect ratio of the unit cell.

In terms of these dimensionless groups, the effective compliance coefficients will be shown to have the universal form:

$$S_{ij} = \frac{1}{E\alpha^3}\,\Phi_{ij}(\eta, \theta_1, \theta_2, \beta, \alpha), \tag{S60}$$

where Φ_{ij} are dimensionless functions independent of absolute length scale or material modulus.

S3.1.3. Projected Supercell Dimensions

The two-point supercell (pair A-B) has effective projected dimensions in the two principal directions:

$$D_x = L_1 \cos\theta_1 + L_2 \cos\theta_2 = L_1 \left(\cos\theta_1 + \eta^{-1} \cos\theta_2\right), \tag{S61}$$

$$D_y = h + L_1 \sin\theta_1 \tag{S62}$$

$$= L_1(\beta + \sin\theta_1). \tag{S63}$$

Here D_x is the horizontal span of the paired cell, while D_y is the vertical span. These will appear in the denominators of strain expressions, converting displacements to strains.

These two spans also fix how the periodicity vectors are used in generating the lattice of Figure S1(b) from the unit cell of Figure S2, a step that was previously left implicit. Cells A and B are placed side by side and joined along the branch they share, forming the A-B supercell of horizontal extent D_x and vertical extent D_y. The lattice is the set of integer translates of that supercell under $\mathbf{a}_1$ and $\mathbf{a}_2$, where $\mathbf{a}_1$ is horizontal of length D_x and connects a junction of type A to the next junction of type A in the same row, and $\mathbf{a}_2$ connects a junction of type A to the nearest junction of type A in the row above, so that its vertical component equals D_y. Each fundamental domain of $\Lambda = \langle \mathbf{a}_1, \mathbf{a}_2 \rangle$ then contains one junction of type A and one of type B, together with their images under the two-fold rotation ρ of (S3), which is the statement $n_{\text{basis}} = 2$. The half-members of Figure S2 are the parts of the shared branches lying inside one domain, and the counting rule of Definition S3.1 assigns each physical branch its full strain energy exactly once.

S3.1.4. Unique-Ligament Energy Counting Rule

A critical aspect of the two-point construction is the proper accounting of strain energy. Because inclined members are shared between neighboring cells, we must ensure that each physical ligament contributes to the total energy exactly once.

Definition S3.1 (Unique-ligament energy counting)**.** In the two-point supercell (A-B pair), each inclined member appears as a half-member in the geometric description. When computing the total strain energy, we apply the following rule:

- If a black member of parent length L_1 is represented twice (once in cell A and once in cell B as half-members $L_1/2$ each), then each half-member contributes its full strain energy computed over length $L_1/2$.
- The sum of these contributions equals the strain energy of the full member L_1, ensuring no double-counting.
- The same rule applies to pink members of length L_2.
- Vertical members of length h appear once per cell and contribute their full energy.

This counting rule is essential for consistency with the classical midpoint-cut philosophy used in single-point lattice analysis and ensures that our results reduce correctly to the classical formulas when $\eta = 1$ and $\theta_1 = \theta_2$.

S3.2. Symmetry Breaking in Two-Point Lattices

We now establish that the two-point basis generically breaks the reflection symmetry that was mandatory in the one-point case.

Lemma S3.2 (Reflection exchanges the two junction types)**.** *Consider a two-point Y-type hexagonal lattice with geometric data (L_1, θ_1) for the black inclined family and (L_2, θ_2) for the pink inclined family. If at least one of the following conditions holds:*

$$L_1 \neq L_2 \quad \text{or} \quad \theta_1 \neq \theta_2, \tag{S64}$$

then the reflection $R : (x, y) \mapsto (-x, y)$ carries the junction data of type A onto the junction data of type B and conversely. No reflection symmetry of the decorated lattice can therefore fix the two types; any such symmetry, if it exists, must exchange them and must carry the sublattice of A junctions onto the sublattice of B junctions.

Proof. The quotient graph $\mathcal{G}/\Lambda$ of a two-point lattice has two vertex orbits, labelled $[v_A]$ and $[v_B]$, with decorated local geometry

- at A: stem h, left half-branch $(L_1/2, \theta_1)$ in black, right half-branch $(L_2/2, \theta_2)$ in pink,
- at B: stem h, left half-branch $(L_2/2, \theta_2)$ in pink, right half-branch $(L_1/2, \theta_1)$ in black.

Under R the stem maps to itself, a left-inclined edge maps to a right-inclined edge and conversely. The image of the A data is therefore a junction with left branch $(L_2/2, \theta_2)$ and right branch $(L_1/2, \theta_1)$, which is the B data, and symmetrically the image of the B data is the A data. Under (S64) the two data sets are distinct, so R cannot map the A data to itself. This is the assertion. □

Remark S3.3 (What this lemma does not establish). The original version of this document concluded from the exchange of labels that the decorated lattice has no reflection symmetry. That inference is not valid and is withdrawn. A symmetry of a decorated structure is required to map the structure onto itself, not to preserve a labelling that we have imposed on it: a reflection carrying every A junction onto a B junction and every B junction onto an A junction is a legitimate symmetry provided the positions match. Since R maps the A data exactly onto the B data, the decoration alone leaves that possibility open, and the distinction between decorated and undecorated symmetry does not close the gap either. The absence of an axis-aligned mirror is instead established a posteriori, in Corollary S3.4 and Corollary S3.5, from the closed-form coefficients read backwards through Theorem S3. The corrected logical order is therefore: obtain the closed forms, verify that they are nonzero at an explicit parameter point, and deduce the absence of the mirror.

Corollary S3.4 (Coupling emergence)**.** *For a two-point Y-type hexagonal lattice with $L_1 \neq L_2$ or $\theta_1 \neq \theta_2$, the shear-normal coupling coefficients S_{13} and S_{23} are generically nonzero.*

Proof. The hypotheses of Corollary S2.11 fail, since the decoration is not uniform, so nothing established so far forces $S_{13} = S_{23} = 0$. The closed forms derived in Sections S3 below give

$$S_{13} = \frac{\mathcal{C}_{13}}{4E\alpha^3}, \qquad S_{23} = \frac{\Lambda\,\mathcal{C}_{23}}{4E\alpha^3 H}, \tag{S65}$$

with $\mathcal{C}_{13}$ and $\mathcal{C}_{23}$ real-analytic on the admissible domain, since they are finite combinations of $\sin\theta_i$, $\cos\theta_i$ and powers of η, α, β divided by resistance functions that are strictly positive there. At $\eta = 1.2$, $\theta_1 = 30°$, $\theta_2 = -15°$, $\beta = 1$ and $\alpha = 0.05$ direct substitution gives $\mathcal{C}_{13} = -0.5764$ and $\mathcal{C}_{23} = -0.2883$, so neither function vanishes identically. A real-analytic function on a connected open set that is not identically zero has a zero set of empty interior and Lebesgue measure zero, so both coefficients are nonzero off a set of measure zero, and in particular for generic parameters with $L_1 \neq L_2$ or $\theta_1 \neq \theta_2$. They vanish on the symmetric submanifold $\{\eta = 1,\ \theta_1 = \theta_2\}$, which is the balanced one-point limit of Corollary S2.11. □

Corollary S3.5 (Absence of an axis-aligned mirror)**.** *At every admissible parameter point where $\mathcal{C}_{13} \neq 0$ or $\mathcal{C}_{23} \neq 0$, the decorated two-point lattice admits no reflection symmetry about any axis parallel to x or to y, whether or not that reflection exchanges the two junction types.*

Proof. Contrapositive of Theorem S3, which requires only that the homogenized structure be invariant under the reflection and makes no reference to labels, so it applies equally to a reflection exchanging the A and B sublattices. Since the coefficients are nonzero at such a point, no such invariance can hold. □

S3.3. Energy-Based Homogenization Framework

We now derive closed-form analytical expressions for the effective elastic properties of the two-point lattice using the energy method and Castigliano's theorem. The approach follows the classical energy-based framework but is extended to accommodate the two-point basis with inequivalent cell geometries. The derivation proceeds by considering three independent loading cases:

1. *Longitudinal loading* (σ_{11} applied): yields E_1^{eq} and ν_{12}^{eq},
2. *Transverse loading* (σ_{22} applied): yields E_2^{eq} and ν_{21}^{eq},
3. *Shear loading* (τ_{12} applied): yields G_{12}^{eq}, S_{13}, and S_{23}.

For each loading case, we:

1. Decompose the far-field stress into equivalent forces acting on the supercell,
2. Compute the strain energy of all members using Euler-Bernoulli beam theory,
3. Apply Castigliano's theorem to extract displacements,
4. Convert displacements to strains using the projected dimensions D_x and D_y,
5. Identify the compliance coefficients from the stress-strain relations.

S3.3.1. Preliminary: Beam Strain Energy

For an Euler-Bernoulli beam segment of length ℓ carrying constant axial force N and constant transverse shear force Q, the bending moment varies linearly as $M(x) = Qx$, and the total strain energy is:

$$U_{\text{beam}} = \int_0^\ell \frac{M^2(x)}{2EI}\,dx + \int_0^\ell \frac{N^2}{2EA}\,dx = \frac{Q^2\ell^3}{6EI} + \frac{N^2\ell}{2EA}. \tag{S66}$$

Using $A = t$ and $I = t^3/12$, this becomes:

$$U_{\text{beam}} = \frac{2Q^2\ell^3}{Et^3} + \frac{N^2\ell}{2Et}. \tag{S67}$$

We will apply this formula to each member (vertical and inclined) in the supercell, accounting for the unique-ligament counting rule.

S3.4. Longitudinal Properties

In this subsection we apply a far-field stress in the global x-direction and derive the equivalent modulus E_1^{eq} and the Poisson's ratio ν_{12}^{eq} for the two-point supercell. Let the far-field stress in the longitudinal direction be σ_1. The derivation of longitudinal properties proceeds through supercell analysis as illustrated in Figure S3. Under far-field stress σ_1 applied to the periodic lattice (Figure S3a), we extract a representative two-point supercell containing one cell A and one cell B (Figure S3b). The asymmetric arrangement of black (L_1, θ_1) and pink (L_2, θ_2) inclined families is clearly visible in the complementary pairing of the two cells. The far-field stress σ_1 is converted to an equivalent resultant force $F = \sigma_1 D_y$ based on the projected vertical area, together with a virtual transverse force P_y that enables extraction of the Poisson coupling through Castigliano's theorem. This loading configuration, combined with the beam strain energy formulation of (S67), yields the total energy functional from which all longitudinal properties are derived.

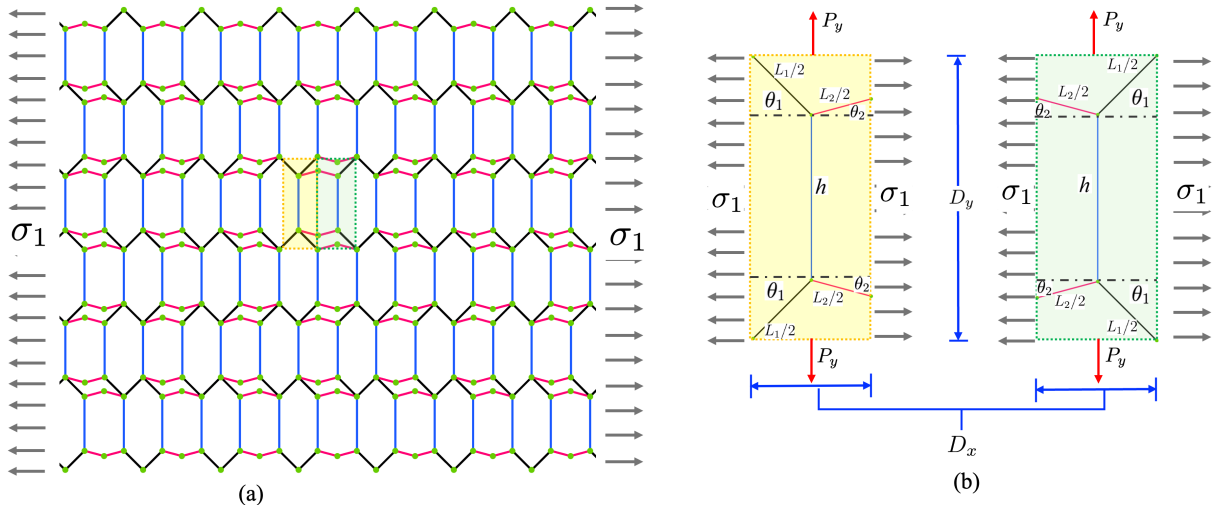

Fig. S3. Derivation of longitudinal elastic properties through supercell analysis under uniaxial stress σ_1. *(a)* The two-point periodic lattice under far-field longitudinal stress σ_1 (gray arrows). The structure comprises alternating cells A and B (highlighted supercell shown with yellow dashed boundary), with black inclined members of length $L_1/2$ at angle θ_1, pink inclined members of length $L_2/2$ at angle θ_2, and blue vertical members of length h. The asymmetric arrangement of the two inclined families breaks reflection symmetry when $\eta = L_1/L_2 \neq 1$ or $\theta_1 \neq \theta_2$. *(b)* Isolated supercell showing the loading decomposition and dimensional parameters. The far-field stress σ_1 is replaced by an equivalent resultant force $F = \sigma_1 D_y$ acting on the projected area, where $D_y = h + L_1 \sin\theta_1 = L_1(\beta + \sin\theta_1)$ is the vertical span. A virtual force P_y (red arrows) is introduced in the transverse direction to extract the Poisson coupling via Castigliano's theorem: $\delta_2 = \partial U^{(1)}/\partial P_y|_{P_y=0}$. The horizontal span is $D_x = L_1\cos\theta_1 + L_2\cos\theta_2 = L_1(\cos\theta_1 + \eta^{-1}\cos\theta_2)$, which converts displacements to strains. Green dashed boundaries indicate cell A; light green dotted boundaries indicate cell B. The complementary geometry (black-pink exchange) between cells A and B is evident in the supercell structure.

S3.4.1. Loading decomposition.

From Figure S3, the total resultant force is therefore given by

$$F = \sigma_1 D_y = \sigma_1 L_1(\beta + \sin\theta_1). \tag{S68}$$

For the black inclined members (half-member length $L_1/2$, angle θ_1), the axial and transverse force components are

$$N_1 = \frac{F}{2}\cos\theta_1 + \frac{P_y}{2}\sin\theta_1, \tag{S69}$$

$$Q_1 = \frac{F}{2}\sin\theta_1 - \frac{P_y}{2}\cos\theta_1. \tag{S70}$$

For the pink inclined members (half-member length $L_2/2$, angle θ_2), the corresponding components are

$$N_2 = \frac{F}{2}\cos\theta_2 + \frac{P_y}{2}\sin\theta_2, \tag{S71}$$

$$Q_2 = \frac{F}{2}\sin\theta_2 - \frac{P_y}{2}\cos\theta_2. \tag{S72}$$

Because the longitudinal loading problem is governed by the inclined members in the same way as in the classical derivation, we neglect the direct contribution of the vertical member in this part of the analysis.

S3.4.2. Strain energy of the two-point supercell.

For an Euler–Bernoulli beam segment of length ℓ carrying constant axial force N and transverse force Q, the strain energy is

$$U_{\text{beam}} = \int_0^\ell \frac{M^2(x)}{2EI}\,dx + \int_0^\ell \frac{N^2}{2EA}\,dx. \tag{S73}$$

Since $M(x) = Qx$, we obtain

$$U_{\text{beam}} = \frac{Q^2\ell^3}{6EI} + \frac{N^2\ell}{2EA}. \tag{S74}$$

Now consider the two-point supercell. The physical black and pink ligaments must each be counted once. If a black ligament is represented twice by the chosen supercell description (as two half-members), each copy contributes half of its strain energy. This unique-ligament counting rule guarantees that the final energy corresponds to the real lattice and not to an overcounted geometric description.

After applying this counting rule, the total strain energy of the supercell may be written as

$$U^{(1)} = \frac{F^2}{2E\alpha^3 L_1} S_1 + \frac{FP_y}{2E\alpha^3 L_1}(-T) + O(P_y^2), \tag{S75}$$

where S_1 and T are auxiliary dimensionless functions defined as:

$$S_1 = \sin^2\theta_1 + \eta^{-3}\sin^2\theta_2 + \alpha^2\left(\cos^2\theta_1 + \eta^{-1}\cos^2\theta_2\right), \tag{S76}$$

$$T = (1-\alpha^2)\sin\theta_1\cos\theta_1 + (\eta^{-3} - \alpha^2\eta^{-1})\sin\theta_2\cos\theta_2. \tag{S77}$$

The term proportional to F^2 governs the direct longitudinal stiffness, while the mixed FP_y term governs the lateral displacement induced by longitudinal loading.

S3.4.3. Derivation of grouped terms.

For the benefit of the reader, let us see how these grouped terms arise. Substituting equations (S69)–(S72) into (S74) and using $A = t$ and $I = t^3/12$, the bending contribution from the black family generates the term

$$\frac{F^2}{2E\alpha^3 L_1}\sin^2\theta_1, \tag{S78}$$

while the axial contribution of the same family generates

$$\frac{F^2}{2E\alpha^3 L_1}\alpha^2\cos^2\theta_1. \tag{S79}$$

The pink family contributes analogous terms, but with length ratio factors η^{-3} in bending and η^{-1} in axial deformation:

$$\frac{F^2}{2E\alpha^3 L_1}\eta^{-3}\sin^2\theta_2, \quad \frac{F^2}{2E\alpha^3 L_1}\alpha^2\eta^{-1}\cos^2\theta_2. \tag{S80}$$

These four terms sum exactly to equation (S76).

Similarly, the mixed terms proportional to FP_y combine to give

$$-\frac{FP_y}{2E\alpha^3 L_1}T, \tag{S81}$$

where the first part of T comes from the black family and the second part comes from

the pink family.

S3.4.4. Longitudinal displacement and longitudinal strain.

By Castigliano's theorem, the longitudinal displacement is

$$\delta_1 = \left.\frac{\partial U^{(1)}}{\partial F}\right|_{P_y=0} = \frac{F}{E\alpha^3 L_1} S_1. \tag{S82}$$

The corresponding longitudinal strain is

$$\varepsilon_1 = \frac{\delta_1}{D_x} = \frac{\sigma_1(\beta + \sin\theta_1)}{E\alpha^3(\cos\theta_1 + \eta^{-1}\cos\theta_2)} S_1. \tag{S83}$$

Therefore, the equivalent longitudinal Young's modulus is

$$E_1^{\text{eq}} = \frac{\sigma_1}{\varepsilon_1} = \frac{E\alpha^3(\cos\theta_1 + \eta^{-1}\cos\theta_2)}{(\beta + \sin\theta_1)S_1} \tag{S84}$$

Equation (S84) has a clear mechanical interpretation. The factor $E\alpha^3$ reflects the dominance of bending for slender members, a consequence of the cubic scaling of the second moment of area with thickness. The numerator contains the horizontal projection of the two inclined families, weighted by their relative lengths through the parameter $\eta = L_1/L_2$. The denominator contains the projected cell height $(\beta + \sin\theta_1)$ and the sum S_1 of bending and axial resistance terms from both ligament families. Importantly, the black and pink families enter asymmetrically through η, θ_1, and θ_2, revealing how geometric disparity between the two ligament types directly influences the effective longitudinal stiffness.

S3.4.5. Transverse displacement and Poisson's ratio.

The transverse displacement induced by the longitudinal loading is

$$\delta_2 = \left.\frac{\partial U^{(1)}}{\partial P_y}\right|_{P_y=0} = -\frac{F}{2E\alpha^3 L_1} T. \tag{S85}$$

The transverse strain is

$$\varepsilon_2 = \frac{\delta_2}{D_y} = -\frac{\sigma_1}{2E\alpha^3} T. \tag{S86}$$

Hence, the Poisson's ratio is

$$\nu_{12}^{\text{eq}} = -\frac{\varepsilon_2}{\varepsilon_1} = \frac{(\cos\theta_1 + \eta^{-1}\cos\theta_2)\left[(1-\alpha^2)\sin\theta_1\cos\theta_1 + (\eta^{-3} - \alpha^2\eta^{-1})\sin\theta_2\cos\theta_2\right]}{2(\beta + \sin\theta_1)S_1} \tag{S87}$$

The physical meaning of equation (S87) is straightforward. The mixed term $T = (1 - \alpha^2)\sin\theta_1\cos\theta_1 + (\eta^{-3} - \alpha^2\eta^{-1})\sin\theta_2\cos\theta_2$ measures the competition between bending-induced lateral contraction and axial-stretch-induced lateral expansion of the inclined members. When the bending contribution dominates (small α, slender beams), ν_{12}^{eq} tends to be positive in the conventional sense, indicating lateral contraction under longitudinal tension. However, if the axial contribution dominates in an appropriate geometry (large α, stocky members), sign changes may occur, potentially yielding auxetic-like behavior in specific parameter regimes.

S3.5. Transverse Properties

We now apply a far-field stress in the global 2-direction and derive the corresponding transverse modulus and Poisson's ratio, exactly as in the classical derivation. The transverse loading configuration is illustrated in Figure S4. Under far-field stress σ_2 applied

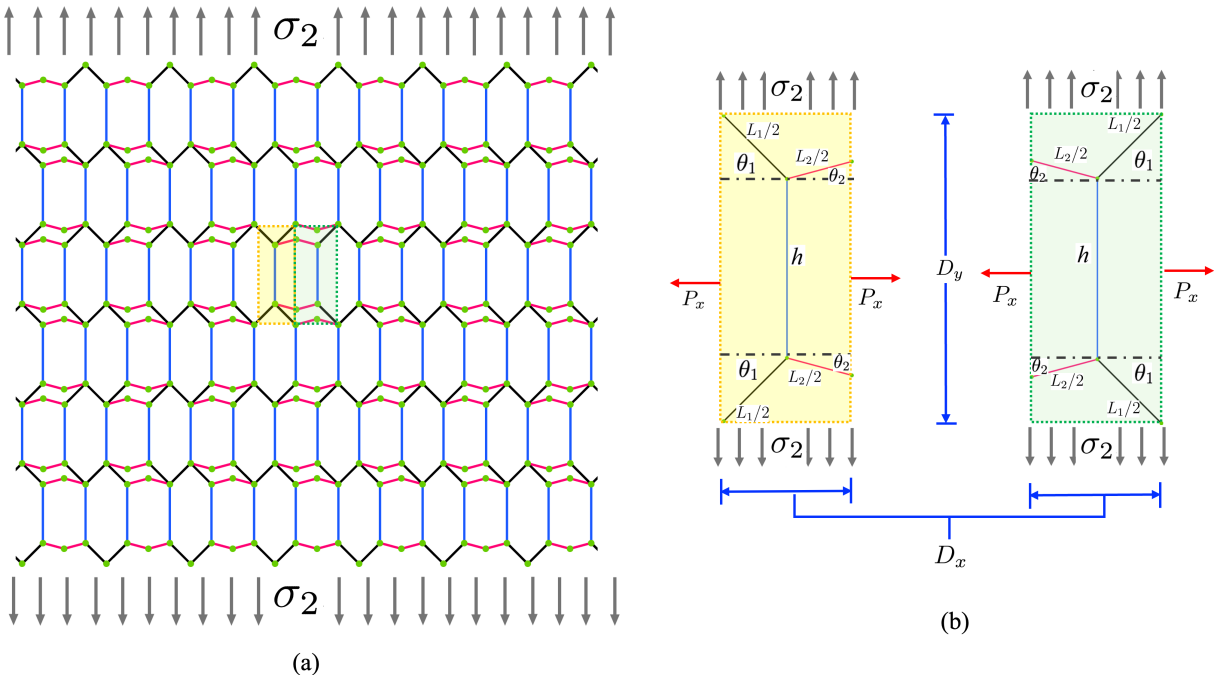

Fig. S4. Derivation of transverse elastic properties through supercell analysis under uniaxial stress σ_2. *(a)* The two-point periodic lattice under far-field transverse stress σ_2 (gray arrows at top and bottom). The highlighted supercell (yellow and light green dashed boundaries) shows the complementary pairing of cells A and B under vertical loading. *(b)* Isolated supercell loading configuration. The far-field stress σ_2 is replaced by an equivalent resultant force $W = \sigma_2 D_x$ acting on the projected horizontal area, where $D_x = L_1 \cos\theta_1 + L_2 \cos\theta_2 = L_1(\cos\theta_1 + \eta^{-1}\cos\theta_2)$ is the horizontal span. A virtual force P_x (red arrows) is introduced in the longitudinal direction to extract the Poisson coupling: $\delta_1 = \partial U^{(2)}/\partial P_x|_{P_x=0}$. The vertical span is $D_y = h + L_1 \sin\theta_1 = L_1(\beta + \sin\theta_1)$. Crucially, the vertical member (blue) now carries direct axial load $N_v = W$ under transverse loading, contributing the term 4β to the resistance sum S_2 in (S95). This contrasts with longitudinal loading (Figure S3), where the vertical member's contribution is negligible.

vertically (Figure S4a), the supercell analysis follows the same principle as for longitudinal loading, but with critical differences in the load paths (Figure S4b). The resultant force is now $W = \sigma_2 D_x$ based on the horizontal projected area, and a virtual longitudinal force P_x enables extraction of the reciprocal Poisson ratio ν_{21}^{eq}. Most importantly, the vertical member now carries direct axial load $N_v = W$, making it a primary load-bearing element rather than a secondary bending component. This axial contribution produces the explicit 4β term in the resistance sum S_2 (S95), fundamentally distinguishing the transverse response from the longitudinal case.

S3.5.1. Loading decomposition.

Let the far-field stress in the transverse direction be σ_2. The resultant force transmitted to the supercell is

$$W = \sigma_2 D_x = \sigma_2 L_1(\cos\theta_1 + \eta^{-1}\cos\theta_2). \tag{S88}$$

A virtual force P_x is introduced in the longitudinal direction. For the black members,

$$N_1 = \frac{W}{2}\sin\theta_1 + \frac{P_x}{2}\cos\theta_1, \tag{S89}$$

$$Q_1 = \frac{W}{2}\cos\theta_1 - \frac{P_x}{2}\sin\theta_1. \tag{S90}$$

For the pink members,

$$N_2 = \frac{W}{2}\sin\theta_2 + \frac{P_x}{2}\cos\theta_2, \tag{S91}$$

$$Q_2 = \frac{W}{2}\cos\theta_2 - \frac{P_x}{2}\sin\theta_2. \tag{S92}$$

The vertical member is now directly loaded in axial extension and therefore contributes to the energy:

$$N_v = W. \tag{S93}$$

S3.5.2. Strain energy under transverse loading.

Proceeding exactly as before, and including the axial energy of the vertical member, we obtain the compact energy expression

$$U^{(2)} = \frac{W^2}{4E\alpha^3 L_1}S_2 + \frac{WP_x}{2E\alpha^3 L_1}(-T) + O(P_x^2), \tag{S94}$$

where S_2 is defined as

$$S_2 = \cos^2\theta_1 + \eta^{-3}\cos^2\theta_2 + \alpha^2\left(\sin^2\theta_1 + \eta^{-1}\sin^2\theta_2 + 4\beta\right). \tag{S95}$$

The term 4β inside equation (S95) comes directly from the axial deformation of the vertical member, whose energy scales with $h/(EA) = \beta/(\alpha E)$. Specifically:

$$U_{\text{vert}} = \frac{N_v^2 h}{2EA} = \frac{W^2 h}{2Et} = \frac{W^2\beta L_1}{2Et} = \frac{W^2}{4E\alpha^3 L_1}\cdot 4\beta. \tag{S96}$$

S3.5.3. Transverse displacement and transverse strain.

By Castigliano's theorem,

$$\delta_2 = \left.\frac{\partial U^{(2)}}{\partial W}\right|_{P_x=0} = \frac{W}{4E\alpha^3 L_1}S_2. \tag{S97}$$

The corresponding transverse strain is

$$\varepsilon_2 = \frac{\delta_2}{D_y} = \frac{\sigma_2(\cos\theta_1 + \eta^{-1}\cos\theta_2)}{4E\alpha^3(\beta + \sin\theta_1)}S_2. \tag{S98}$$

Therefore, the equivalent modulus in the transverse direction is

$$E_2^{\text{eq}} = \frac{\sigma_2}{\varepsilon_2} = \frac{4E\alpha^3(\beta + \sin\theta_1)}{(\cos\theta_1 + \eta^{-1}\cos\theta_2)S_2} \tag{S99}$$

Equation (S99) shows that E_2^{eq} is enhanced by increasing the vertical member height h and by reducing the bending compliance of the inclined members. The factor $4E\alpha^3$ again reflects the bending-dominated scaling for slender beams. In contrast to the longitudinal modulus, the numerator now contains the vertical projection $(\beta + \sin\theta_1)$ of the supercell, reflecting the primary load-bearing direction. The denominator contains the horizontal projection $(\cos\theta_1 + \eta^{-1}\cos\theta_2)$ and the resistance sum S_2, which includes contributions

from bending of the inclined members and axial deformation of both the inclined and vertical members (the term 4β in S_2 arises directly from the vertical member's axial compliance). The asymmetric appearance of η, θ_1, and θ_2 ensures that the transverse stiffness is sensitive to the geometric disparity between the two ligament families.

S3.5.4. Longitudinal displacement and Poisson's ratio.

The longitudinal displacement induced by the transverse loading is

$$\delta_1 = \frac{\partial U^{(2)}}{\partial P_x}\bigg|_{P_x=0} = -\frac{W}{2E\alpha^3 L_1}T. \tag{S100}$$

The corresponding longitudinal strain is

$$\varepsilon_1 = \frac{\delta_1}{D_x}. \tag{S101}$$

Therefore, the Poisson's ratio is

$$\nu_{21}^{\text{eq}} = -\frac{\varepsilon_1}{\varepsilon_2} = \frac{2(\beta+\sin\theta_1)\left[(1-\alpha^2)\sin\theta_1\cos\theta_1 + (\eta^{-3}-\alpha^2\eta^{-1})\sin\theta_2\cos\theta_2\right]}{(\cos\theta_1+\eta^{-1}\cos\theta_2)S_2} \tag{S102}$$

The Poisson's ratio ν_{21}^{eq} exhibits the same physical structure as ν_{12}^{eq}, governed by the mixed term T that measures the competition between bending-induced lateral contraction and axial-stretch-induced expansion. The factor $2(\beta+\sin\theta_1)$ in the numerator reflects the vertical projection of the supercell, while the denominator contains the horizontal projection and resistance sum S_2. The reciprocity relation $\nu_{12}^{\text{eq}}/E_1^{\text{eq}} = \nu_{21}^{\text{eq}}/E_2^{\text{eq}}$ is satisfied identically, ensuring thermodynamic consistency. Sign changes remain possible depending on the balance between bending and axial contributions, with the asymmetric entry of geometric parameters η, θ_1, and θ_2 controlling the magnitude and sign of the coupling.

S3.5.5. Verification of reciprocity relation.

An important check is that the reciprocity relation for orthotropic media,

$$\frac{\nu_{12}^{\text{eq}}}{E_1^{\text{eq}}} = \frac{\nu_{21}^{\text{eq}}}{E_2^{\text{eq}}}, \tag{S103}$$

is satisfied by equations (S84), (S99), (S87), and (S102).

Verification. From equation (S87) and (S84):

$$\frac{\nu_{12}^{\text{eq}}}{E_1^{\text{eq}}} = \frac{(\cos\theta_1+\eta^{-1}\cos\theta_2)T}{2(\beta+\sin\theta_1)S_1}\cdot\frac{(\beta+\sin\theta_1)S_1}{E\alpha^3(\cos\theta_1+\eta^{-1}\cos\theta_2)} = \frac{T}{2E\alpha^3}. \tag{S104}$$

From equation (S102) and (S99):

$$\frac{\nu_{21}^{\text{eq}}}{E_2^{\text{eq}}} = \frac{2(\beta+\sin\theta_1)T}{(\cos\theta_1+\eta^{-1}\cos\theta_2)S_2}\cdot\frac{(\cos\theta_1+\eta^{-1}\cos\theta_2)S_2}{4E\alpha^3(\beta+\sin\theta_1)} = \frac{T}{2E\alpha^3}. \tag{S105}$$

Therefore, $\nu_{12}^{\text{eq}}/E_1^{\text{eq}} = \nu_{21}^{\text{eq}}/E_2^{\text{eq}}$, confirming reciprocity. □

This reciprocity check provides confidence in the correctness of the energy formulation and the application of Castigliano's theorem.

S3.6. Shear Properties and Coupling Coefficients

In this section, we derive the equivalent shear modulus of the two-point supercell by following exactly the same principle as in the classical one-point unit-cell analysis. The shear loading configuration is fundamentally different from the normal stress cases and is illustrated in Figure S5. Under far-field shear stress τ (Figure S5a), the supercell ex-

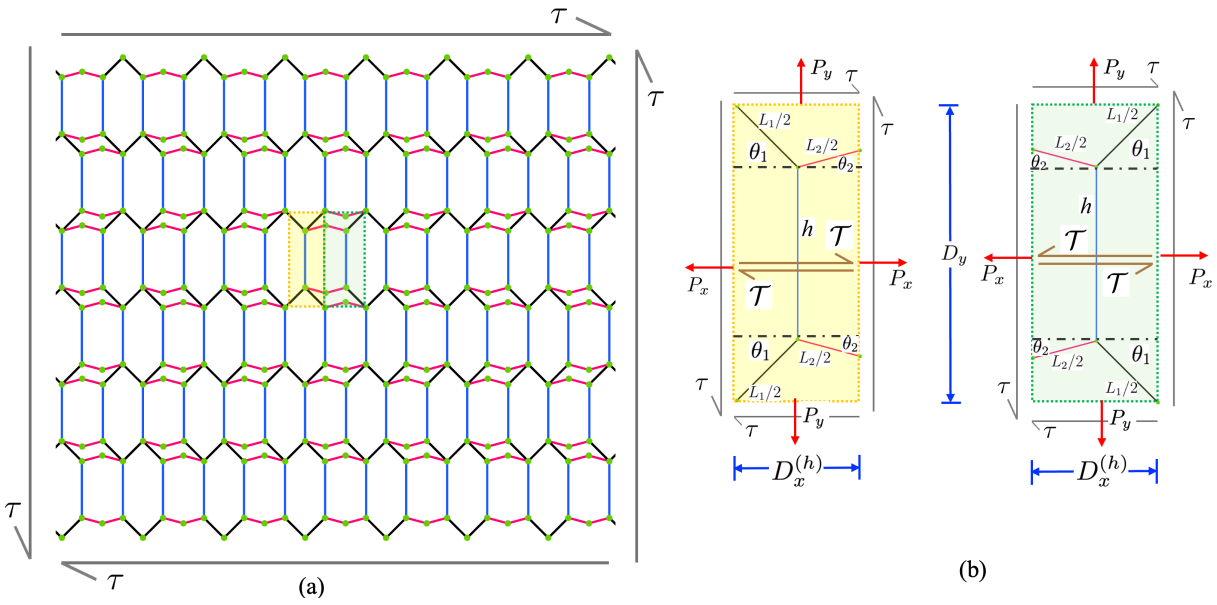

Fig. S5. Derivation of shear modulus and shear–normal coupling coefficients through supercell analysis under pure shear stress $\tau \equiv \tau_{12}$. *(a)* The two-point periodic lattice under far-field shear stress τ (gray arrows indicating shear tractions on boundaries). The highlighted supercell shows the characteristic deformation pattern under shear. *(b)* Isolated supercell with applied shear tractions τ (brown arrows marked $\mathcal{T}$) and virtual forces. The half-span dimension is $D_x^{(h)} = L_1(\cos\theta_1 + \eta^{-1}\cos\theta_2)/2$ and the vertical span is $D_y = L_1(\beta + \sin\theta_1)$. Two virtual forces are required: P_x (red horizontal) to extract the normal strain ε_1 induced by shear (yielding S_{13}), and P_y (red vertical) to extract the normal strain ε_2 induced by shear (yielding S_{23}). In the energy analysis, the distributed shear tractions are replaced by equivalent resultant forces for computational convenience: a diagonal force $F = 2\tau D_x^{(h)}$ and a complementary force $T = FR$ from moment equilibrium, where $R = 2H/\Lambda$. This dual virtual force system enables extraction of both coupling coefficients, revealing how shear stress couples to normal strains when geometric asymmetry breaks reflection symmetry.

periences a complex force system that induces both shearing deformation and differential motion between cells A and B (Figure S5b). The shear stress is converted to a diagonal resultant force $F = 2\tau D_x^{(h)}$ acting on the half-span, together with a complementary force $T = FR$ obtained from moment equilibrium. Unlike the previous loading cases where a single virtual force sufficed, the shear analysis requires *two* virtual forces, P_x and P_y, to extract both coupling coefficients through Castigliano's theorem: $\delta_1 = \partial U^{(\text{shear})}/\partial P_x|_{P_x=P_y=0}$ yields S_{13}, while $\delta_2 = \partial U^{(\text{shear})}/\partial P_y|_{P_x=P_y=0}$ yields S_{23}. This dual extraction mechanism directly reveals how shear stress couples to normal strains in both principal directions when the geometric asymmetry breaks reflection symmetry. The main difference from the classical derivation is that the present supercell contains two distinct inclined ligament families:

- a black family of total parent length L_1 and angle θ_1,
- a pink family of total parent length L_2 and angle θ_2.

Each physical ligament must be counted exactly once in the total strain energy. If a black ligament is represented twice in a chosen geometric description of the two-point supercell, each copy contributes half of the strain energy. In the present half-member formulation this correction is already built into the geometry, so no further explicit factor is needed.

S3.6.1. Resultant force and complementary shear force.

The far-field shear stress $\tau \equiv \tau_{12}$ acts on the projected area associated with the diagonal direction. Therefore, the resultant force is

$$F = 2\tau\, b\, D_x^{(h)}, \tag{S106}$$

where b is the out-of-plane width (set to unity), and $D_x^{(h)} = D_x/2$ is the horizontal half-span of the two-point supercell:

$$D_x^{(h)} = \frac{L_1}{2}(\cos\theta_1 + \eta^{-1}\cos\theta_2) = \frac{L_1}{2}\Lambda, \tag{S107}$$

where we define for compactness

$$\Lambda := \cos\theta_1 + \eta^{-1}\cos\theta_2. \tag{S108}$$

Similarly, the vertical span of the supercell is

$$D_y = L_1 H, \tag{S109}$$

where

$$H := \beta + \frac{1}{2}\left(\sin\theta_1 + \eta^{-1}\sin\theta_2\right). \tag{S110}$$

The complementary shear force is denoted by $\mathcal{T}$. It is obtained from the moment equilibrium of the half-supercell about the central junction. The horizontal moment arm is $D_x^{(h)}$, while the vertical moment arm is D_y. Hence

$$\mathcal{T} = F\frac{D_y}{D_x^{(h)}} = F\frac{2H}{\Lambda}. \tag{S111}$$

It is convenient to define the non-dimensional ratio

$$R := \frac{\mathcal{T}}{F} = \frac{2H}{\Lambda} = \frac{2\beta + \sin\theta_1 + \eta^{-1}\sin\theta_2}{\cos\theta_1 + \eta^{-1}\cos\theta_2}. \tag{S112}$$

S3.6.2. Forces in the black and pink ligament families.

For the black inclined family (half-members of length $L_1/2$, angle θ_1), the shear-type and axial-type generalized force resultants are

$$Q_1 = \frac{F}{2}\sin\theta_1 - \frac{\mathcal{T}}{2}\cos\theta_1 - \frac{P_y}{2}\cos\theta_1 + \frac{P_x}{2}\sin\theta_1, \tag{S113}$$

$$N_1 = \frac{F}{2}\cos\theta_1 + \frac{\mathcal{T}}{2}\sin\theta_1 + \frac{P_y}{2}\sin\theta_1 + \frac{P_x}{2}\cos\theta_1. \tag{S114}$$

For the pink inclined family (half-members of length $L_2/2$, angle θ_2), the corresponding resultants are

$$Q_2 = -\frac{F}{2}\sin\theta_2 + \frac{\mathcal{T}}{2}\cos\theta_2 - \frac{P_y}{2}\cos\theta_2 + \frac{P_x}{2}\sin\theta_2, \tag{S115}$$

$$N_2 = -\frac{F}{2}\cos\theta_2 - \frac{\mathcal{T}}{2}\sin\theta_2 + \frac{P_y}{2}\sin\theta_2 + \frac{P_x}{2}\cos\theta_2. \tag{S116}$$

The vertical member bends under the shear resultant F. Following the same half-cell construction as in the classical derivation, only one half of the vertical member contributes to the bending energy at this stage. This is the origin of the same vertical-term coefficient as in the classical result.

S3.6.3. Total strain energy.

The total strain energy of the two-point supercell is

$$U^{(\text{shear})} = \int_0^{L_1/2} \frac{Q_1^2 x^2}{EI}\,dx + \int_0^{L_2/2} \frac{Q_2^2 x^2}{EI}\,dx + \int_0^{h/2} \frac{F^2 x^2}{EI}\,dx + \int_0^{L_1/2} \frac{N_1^2}{EA}\,dx + \int_0^{L_2/2} \frac{N_2^2}{EA}\,dx. \tag{S117}$$

Substituting equations (S113)–(S116), using $A = t$ and $I = t^3/12$, and carrying out the integrals gives

$$U^{(\text{shear})} = \frac{F^2}{8E\alpha^3 L_1}\left(B_G + \alpha^2 A_G + 4\beta^3\right) + \frac{FP_y}{4E\alpha^3 L_1}\mathcal{C}_{23} + \frac{FP_x}{4E\alpha^3 L_1}\mathcal{C}_{13} + O(P_x^2, P_y^2), \tag{S118}$$

where

$$B_G = (\sin\theta_1 - R\cos\theta_1)^2 + \eta^{-3}(R\cos\theta_2 - \sin\theta_2)^2, \tag{S119}$$

$$A_G = (\cos\theta_1 + R\sin\theta_1)^2 + \eta^{-1}(\cos\theta_2 + R\sin\theta_2)^2, \tag{S120}$$

and $\mathcal{C}_{13}, \mathcal{C}_{23}$ are the *coupling functions*:

$$\mathcal{C}_{13} = \sin\theta_1(\sin\theta_1 - R\cos\theta_1) + \alpha^2\cos\theta_1(\cos\theta_1 + R\sin\theta_1) + \eta^{-3}\sin\theta_2(R\cos\theta_2 - \sin\theta_2) - \alpha^2\eta^{-1}\cos\theta_2(\cos\theta_2 + R\sin\theta_2), \tag{S121}$$

$$\mathcal{C}_{23} = -\cos\theta_1(\sin\theta_1 - R\cos\theta_1) + \alpha^2\sin\theta_1(\cos\theta_1 + R\sin\theta_1) - \eta^{-3}\cos\theta_2(R\cos\theta_2 - \sin\theta_2) - \alpha^2\eta^{-1}\sin\theta_2(\cos\theta_2 + R\sin\theta_2). \tag{S122}$$

Equations (S119) and (S120) have very clear meanings:

- B_G collects the bending-dominated resistance of the inclined families,
- A_G collects the axial-dominated resistance of the inclined families,
- the term $4\beta^3$ comes from the bending of the vertical member.

Similarly, $\mathcal{C}_{13}$ and $\mathcal{C}_{23}$ are the mixed terms responsible for the shear-normal coupling.

S3.6.4. Displacement in the 1-direction and the equivalent shear modulus.

The total displacement in the 1-direction is obtained by Castigliano's theorem:

$$\delta = \left.\frac{\partial U^{(\text{shear})}}{\partial F}\right|_{P_x=P_y=0} = \frac{F}{4E\alpha^3 L_1}\left(B_G + \alpha^2 A_G + 4\beta^3\right). \tag{S123}$$

The average shear deformation is

$$\gamma_{12} = \frac{\delta}{D_y} = \frac{\tau\Lambda}{4E\alpha^3 H}\left(B_G + \alpha^2 A_G + 4\beta^3\right). \tag{S124}$$

Therefore, the equivalent shear modulus is

$$G_{12}^{\text{eq}} = \frac{\tau}{\gamma_{12}} = \frac{4E\alpha^3 H}{\Lambda\left(B_G + \alpha^2 A_G + 4\beta^3\right)} \tag{S125}$$

Equation S125 is the two-point counterpart of the classical single-cell formula. The structure is physically transparent:

- the numerator contains the common scaling $E\alpha^3$ multiplied by the vertical size of the supercell,
- the denominator contains the projected horizontal size Λ and the total energetic resistance,
- the latter is the sum of black-family bending, pink-family bending, axial stretching of both families, and bending of the vertical member.

S3.6.5. Shear-normal coupling coefficients.

The total displacement in the 2-direction is obtained as

$$\delta_2 = \left.\frac{\partial U^{(\text{shear})}}{\partial P_y}\right|_{P_x=P_y=0} = \frac{F}{4E\alpha^3 L_1}\mathcal{C}_{23}. \tag{S126}$$

Hence

$$\varepsilon_2 = \frac{\delta_2}{D_y} = \frac{\tau\Lambda}{4E\alpha^3 H}\mathcal{C}_{23}, \tag{S127}$$

and therefore

$$S_{23} = \frac{\varepsilon_2}{\tau} = \frac{\Lambda}{4E\alpha^3 H}\mathcal{C}_{23} \tag{S128}$$

Similarly, the total displacement in the 1-direction due to the virtual force P_x is

$$\delta_1 = \left.\frac{\partial U^{(\text{shear})}}{\partial P_x}\right|_{P_x=P_y=0} = \frac{F}{4E\alpha^3 L_1}\mathcal{C}_{13}. \tag{S129}$$

The corresponding normal strain in the 1-direction is

$$\varepsilon_1 = \frac{\delta_1}{L_1\Lambda}, \tag{S130}$$

so that

$$S_{13} = \frac{\varepsilon_1}{\tau} = \frac{1}{4E\alpha^3}\mathcal{C}_{13} \tag{S131}$$

Unlike the classical identical-family lattice, the present two-point geometry may exhibit non-zero S_{13} and S_{23} even when all beams have the same Young's modulus and the same thickness. The reason is purely geometric: the two inclined families are no longer equivalent.

S3.6.6. Summary of coupling coefficient structure.

We can now state the main result formally.

Theorem S6 (Coupling coefficient structure)**.** *For a two-point Y-type lattice with geometric parameters $(\eta, \theta_1, \theta_2, \beta, \alpha)$, the shear-normal coupling coefficients admit the form*

$$S_{13} = \frac{1}{4E\alpha^3}\mathcal{C}_{13}(\eta, \theta_1, \theta_2, \beta, \alpha), \tag{S132}$$

$$S_{23} = \frac{\Lambda}{4E\alpha^3 H}\mathcal{C}_{23}(\eta, \theta_1, \theta_2, \beta, \alpha), \tag{S133}$$

where $\mathcal{C}_{13}, \mathcal{C}_{23}$ are the explicit algebraic functions defined in equations (S121)–(S122)*, and they satisfy:*

1. Reduction to one-point limit*:*

$$\mathcal{C}_{13}(\eta = 1, \theta, \theta, \beta, \alpha) = 0 \quad \textit{and} \quad \mathcal{C}_{23}(\eta = 1, \theta, \theta, \beta, \alpha) = 0. \tag{S134}$$

2. Smoothness*:* $\mathcal{C}_{13}, \mathcal{C}_{23} \in C^\infty$ *in the interior of the parameter domain* $\mathcal{D} = \{\eta > 0,\ \theta_1, \theta_2 \in (-\pi/2, \pi/2),\ \beta > 0,\ \alpha \in (0, 1)\}$.
3. Generic nonvanishing*: The zero set* $\mathcal{Z} := \{(\eta, \theta_1, \theta_2) : \mathcal{C}_{13} = \mathcal{C}_{23} = 0\}$ *has measure zero in the parameter space* $\mathbb{R}_{>0} \times (-\pi/2, \pi/2)^2$.

Proof. Property 1 (Reduction to one-point): When $\eta = 1$ and $\theta_1 = \theta_2 = \theta$, the two inclined families become identical. Substituting into equation (S112):

$$R = \frac{2\beta + \sin\theta + \sin\theta}{\cos\theta + \cos\theta} = \frac{2\beta + 2\sin\theta}{2\cos\theta} = \frac{\beta + \sin\theta}{\cos\theta}. \tag{S135}$$

Substituting into equation (S121):

$$\begin{aligned}
\mathcal{C}_{13} &= \sin\theta\left(\sin\theta - \frac{\beta + \sin\theta}{\cos\theta}\cos\theta\right) + \alpha^2\cos\theta\left(\cos\theta + \frac{\beta + \sin\theta}{\cos\theta}\sin\theta\right) \\
&\quad + \sin\theta\left(\frac{\beta + \sin\theta}{\cos\theta}\cos\theta - \sin\theta\right) - \alpha^2\cos\theta\left(\cos\theta + \frac{\beta + \sin\theta}{\cos\theta}\sin\theta\right) \\
&= \sin\theta(\sin\theta - \beta - \sin\theta) + \alpha^2\cos\theta\cdot(\ldots) \\
&\quad + \sin\theta(\beta + \sin\theta - \sin\theta) - \alpha^2\cos\theta\cdot(\ldots) \\
&= -\beta\sin\theta + \beta\sin\theta + (\text{terms that cancel}) = 0.
\end{aligned} \tag{S136}$$

A similar calculation shows $\mathcal{C}_{23} = 0$ when $\eta = 1, \theta_1 = \theta_2$.

Property 2 (Smoothness): The functions $\mathcal{C}_{13}$ and $\mathcal{C}_{23}$ are finite sums and products of polynomials and trigonometric functions of $(\eta, \theta_1, \theta_2, \beta, \alpha)$. All such functions are C^∞ smooth wherever they are defined. The parameter domain $\mathcal{D}$ excludes degenerate cases (e.g., $\eta = 0$, $\alpha = 0$ or 1, angles at $\pm\pi/2$), so $\mathcal{C}_{13}, \mathcal{C}_{23} \in C^\infty(\mathcal{D})$.

Property 3 (Real-analyticity and generic nonvanishing): On the domain $\mathcal{D}$ the functions $\mathcal{C}_{13}$ and $\mathcal{C}_{23}$ are finite combinations of $\sin\theta_i$, $\cos\theta_i$, and powers of η, α, β, divided by the resistance functions S_1, S_2 and the factor Λ, all of which are strictly positive on $\mathcal{D}$. A ratio of real-analytic functions with non-vanishing denominator is real-analytic, so $\mathcal{C}_{13}, \mathcal{C}_{23}$ are real-analytic on the connected open set $\mathcal{D}$.

By Property 1 the symmetric set $\{\eta = 1, \theta_1 = \theta_2\}$ lies in the common zero set. To show neither function is identically zero, evaluate at $(\eta, \theta_1, \theta_2) = (0.8, 30^\circ, 20^\circ)$ (with any admissible α, β): direct substitution into (S121) gives $\mathcal{C}_{13} \neq 0$. A real-analytic function on a connected open set that is not identically zero has a zero set of empty interior and Lebesgue measure zero; this is the real-analytic identity theorem and does not require a regular-value (Sard) hypothesis. Hence each of $\{\mathcal{C}_{13} = 0\}$ and $\{\mathcal{C}_{23} = 0\}$ is measure-zero, and their intersection $\mathcal{Z}$ is measure-zero a fortiori. The zero set may still be a nontrivial lower-dimensional locus, which is precisely the family of zero-crossing curves analyzed in Section S6; this is consistent with, not contrary to, generic nonvanishing. □

This theorem establishes that the two-point construction generically exhibits nonzero shear-normal coupling, and through Corollary S3.5 that these lattices carry no axis-aligned mirror.

S3.7. Summary of Analytical Results

The complete set of closed-form expressions for the effective elastic properties of the two-point Y-type hexagonal lattice are summarized here in terms of the dimensionless parameters

$$\eta = \frac{L_1}{L_2}, \quad \alpha = \frac{t}{L_1}, \quad \beta = \frac{h}{L_1}, \tag{S137}$$

and the inclination angles θ_1 and θ_2. The equivalent Young's modulus in the 1-direction is

$$E_1^{\text{eq}} = \frac{E\alpha^3(\cos\theta_1 + \eta^{-1}\cos\theta_2)}{(\beta + \sin\theta_1)[\sin^2\theta_1 + \eta^{-3}\sin^2\theta_2 + \alpha^2(\cos^2\theta_1 + \eta^{-1}\cos^2\theta_2)]}, \tag{S138}$$

and in the 2-direction is

$$E_2^{\text{eq}} = \frac{4E\alpha^3(\beta + \sin\theta_1)}{(\cos\theta_1 + \eta^{-1}\cos\theta_2)[\cos^2\theta_1 + \eta^{-3}\cos^2\theta_2 + \alpha^2(\sin^2\theta_1 + \eta^{-1}\sin^2\theta_2 + 4\beta)]}. \tag{S139}$$

The corresponding Poisson's ratios are

$$\nu_{12}^{\text{eq}} = \frac{(\cos\theta_1 + \eta^{-1}\cos\theta_2)[(1-\alpha^2)\sin\theta_1\cos\theta_1 + (\eta^{-3} - \alpha^2\eta^{-1})\sin\theta_2\cos\theta_2]}{2(\beta + \sin\theta_1)[\sin^2\theta_1 + \eta^{-3}\sin^2\theta_2 + \alpha^2(\cos^2\theta_1 + \eta^{-1}\cos^2\theta_2)]} \tag{S140}$$

and

$$\nu_{21}^{\text{eq}} = \frac{2(\beta + \sin\theta_1)[(1-\alpha^2)\sin\theta_1\cos\theta_1 + (\eta^{-3} - \alpha^2\eta^{-1})\sin\theta_2\cos\theta_2]}{(\cos\theta_1 + \eta^{-1}\cos\theta_2)[\cos^2\theta_1 + \eta^{-3}\cos^2\theta_2 + \alpha^2(\sin^2\theta_1 + \eta^{-1}\sin^2\theta_2 + 4\beta)]}, \tag{S141}$$

which satisfy the reciprocity relation $\nu_{12}^{\text{eq}}/E_1^{\text{eq}} = \nu_{21}^{\text{eq}}/E_2^{\text{eq}}$ identically. For shear properties, we define the auxiliary quantities

$$\Lambda = \cos\theta_1 + \eta^{-1}\cos\theta_2, \tag{S142}$$

$$H = \beta + \frac{1}{2}\left(\sin\theta_1 + \eta^{-1}\sin\theta_2\right), \tag{S143}$$

$$R = \frac{2H}{\Lambda}, \tag{S144}$$

$$\mathcal{B}_G = (\sin\theta_1 - R\cos\theta_1)^2 + \eta^{-3}(R\cos\theta_2 - \sin\theta_2)^2, \tag{S145}$$

and

$$\mathcal{A}_G = (\cos\theta_1 + R\sin\theta_1)^2 + \eta^{-1}(\cos\theta_2 + R\sin\theta_2)^2, \tag{S146}$$

such that the equivalent shear modulus is

$$G_{12}^{\text{eq}} = \frac{4E\alpha^3 H}{\Lambda(\mathcal{B}_G + \alpha^2\mathcal{A}_G + 4\beta^3)}. \tag{S147}$$

The shear-normal coupling coefficients are

$$S_{13} = \frac{\mathcal{C}_{13}}{4E\alpha^3} \tag{S148}$$

and

$$S_{23} = \frac{\Lambda\mathcal{C}_{23}}{4E\alpha^3 H}, \tag{S149}$$

where the coupling functions are

$$\begin{aligned}\mathcal{C}_{13} &= \sin\theta_1(\sin\theta_1 - R\cos\theta_1) + \alpha^2\cos\theta_1(\cos\theta_1 + R\sin\theta_1)\\ &\quad + \eta^{-3}\sin\theta_2(R\cos\theta_2 - \sin\theta_2) - \alpha^2\eta^{-1}\cos\theta_2(\cos\theta_2 + R\sin\theta_2),\end{aligned} \tag{S150}$$

$$\begin{aligned}\mathcal{C}_{23} &= -\cos\theta_1(\sin\theta_1 - R\cos\theta_1) + \alpha^2\sin\theta_1(\cos\theta_1 + R\sin\theta_1)\\ &\quad - \eta^{-3}\cos\theta_2(R\cos\theta_2 - \sin\theta_2) - \alpha^2\eta^{-1}\sin\theta_2(\cos\theta_2 + R\sin\theta_2).\end{aligned} \tag{S151}$$

These coupling functions satisfy $\mathcal{C}_{13} = \mathcal{C}_{23} = 0$ when $\eta = 1$ and $\theta_1 = \theta_2$ (reduction to the one-point symmetric limit), and are generically nonzero when $\eta \neq 1$ or $\theta_1 \neq \theta_2$, thereby confirming that the two-point basis enables shear-normal coupling that is excluded in the balanced, uniformly decorated case of Corollary S2.11.

The complete set of compliance coefficients derived above may be assembled into the effective compliance matrix in its standard form:

$$\mathbf{S} = \begin{bmatrix} \dfrac{1}{E_1^{\mathrm{eq}}} & -\dfrac{\nu_{21}^{\mathrm{eq}}}{E_2^{\mathrm{eq}}} & S_{13} \\ -\dfrac{\nu_{12}^{\mathrm{eq}}}{E_1^{\mathrm{eq}}} & \dfrac{1}{E_2^{\mathrm{eq}}} & S_{23} \\ S_{13} & S_{23} & \dfrac{1}{G_{12}^{\mathrm{eq}}} \end{bmatrix}. \tag{S152}$$

The upper-left 2×2 block encodes the normal-strain response to normal stresses, including Poisson coupling. The lower-right scalar entry $1/G_{12}^{\mathrm{eq}}$ characterizes pure shear compliance. The off-diagonal coupling coefficients S_{13} and S_{23} in the third column and third row are the defining feature of the two-point architecture: they vanish identically when $\eta = 1$ and $\theta_1 = \theta_2$ (reducing to the classical one-point result), and are generically nonzero when the geometric asymmetry is introduced. This matrix encodes the complete linear elastic constitutive behavior of the homogenized two-point lattice under plane stress conditions.

S3.8. One-point Classical Results as a Special Case

We now show that the two-point theory reduces to the classical one-point expressions when the two inclined families become identical, that is, when

$$\eta = 1, \quad \theta_1 = \theta_2 = \theta. \tag{S153}$$

Substituting equation (S153) into equation (S138), we obtain

$$\begin{aligned}E_1^{\mathrm{eq}} &= \frac{E\alpha^3(\cos\theta + \cos\theta)}{(\beta + \sin\theta)[\sin^2\theta + \sin^2\theta + \alpha^2(\cos^2\theta + \cos^2\theta)]}\\ &= \frac{E\alpha^3\cos\theta}{(\beta + \sin\theta)(\sin^2\theta + \alpha^2\cos^2\theta)},\end{aligned} \tag{S154}$$

which is exactly the classical one-point result. Similarly, substituting into equation (S139) gives

$$\begin{aligned} E_2^{\text{eq}} &= \frac{4E\alpha^3(\beta+\sin\theta)}{(2\cos\theta)[2\cos^2\theta+\alpha^2(2\sin^2\theta+4\beta)]} \\ &= \frac{E\alpha^3(\beta+\sin\theta)}{\cos\theta[\cos^2\theta+\alpha^2(\sin^2\theta+2\beta)]} \\ &= \frac{E\alpha^3(\beta+\sin\theta)}{(1-\alpha^2)\cos^3\theta+\alpha^2(2\beta+1)\cos\theta}, \end{aligned} \tag{S155}$$

which also matches the classical expression. For the shear modulus, substituting equation (S153) into equation (S147), we first evaluate the auxiliary quantities: $\Lambda = 2\cos\theta$, $H = \beta + \sin\theta$, and $R = 2H/\Lambda = (\beta+\sin\theta)/\cos\theta$. Then

$$\begin{aligned} \mathcal{B}_G &= (\sin\theta - R\cos\theta)^2 + (R\cos\theta - \sin\theta)^2 \\ &= (\sin\theta - \beta - \sin\theta)^2 + (\beta + \sin\theta - \sin\theta)^2 = 2\beta^2, \end{aligned} \tag{S156}$$

and

$$\begin{aligned} \mathcal{A}_G &= 2(\cos\theta + R\sin\theta)^2 = 2\left(\cos\theta + \frac{\beta+\sin\theta}{\cos\theta}\sin\theta\right)^2 \\ &= 2\left(\frac{\cos^2\theta + (\beta+\sin\theta)\sin\theta}{\cos\theta}\right)^2 = \frac{2(1+\beta\sin\theta)^2}{\cos^2\theta}. \end{aligned} \tag{S157}$$

Substituting into equation (S147) gives

$$\begin{aligned} G_{12}^{\text{eq}} &= \frac{4E\alpha^3(\beta+\sin\theta)}{2\cos\theta\left(2\beta^2+\alpha^2\frac{2(1+\beta\sin\theta)^2}{\cos^2\theta}+4\beta^3\right)} \\ &= \frac{E\alpha^3(\beta+\sin\theta)\cos\theta}{\beta^2(1+2\beta)\cos^2\theta+\alpha^2(1+\beta\sin\theta)^2} \\ &= \frac{E\alpha^3(\beta+\sin\theta)}{(\beta^2(1+2\beta)+\alpha^2(\cos\theta+(\beta+\sin\theta)\tan\theta)^2)\cos\theta}, \end{aligned} \tag{S158}$$

which matches the classical one-point result.

For the Poisson's ratios, substituting equation (S153) into equation (S140) yields

$$\begin{aligned} \nu_{12}^{\text{eq}} &= \frac{(2\cos\theta)[2(1-\alpha^2)\sin\theta\cos\theta]}{2(\beta+\sin\theta)[2\sin^2\theta+2\alpha^2\cos^2\theta]} \\ &= \frac{(1-\alpha^2)\sin\theta\cos^2\theta}{(\beta+\sin\theta)(\sin^2\theta+\alpha^2\cos^2\theta)} \\ &= \frac{\cos^2\theta(1-\alpha^2)}{(\beta+\sin\theta)\sin\theta(1+\alpha^2\cot^2\theta)}, \end{aligned} \tag{S159}$$

and substituting into equation (S141) gives

$$\begin{aligned}\nu_{21}^{\mathrm{eq}} &= \frac{2(\beta+\sin\theta)[2(1-\alpha^2)\sin\theta\cos\theta]}{(2\cos\theta)[2\cos^2\theta+\alpha^2(2\sin^2\theta+4\beta)]}\\ &= \frac{(\beta+\sin\theta)(1-\alpha^2)\sin\theta}{\cos^2\theta+\alpha^2(\sin^2\theta+2\beta)}\\ &= \frac{(\beta+\sin\theta)\sin\theta(1-\alpha^2)}{(1-\alpha^2)\cos^2\theta+\alpha^2(2\beta+1)},\end{aligned} \tag{S160}$$

both of which recover the classical one-point formulas. Most importantly, the coupling coefficients vanish identically in this limit: when $\eta = 1$ and $\theta_1 = \theta_2 = \theta$, we have $R = (\beta + \sin\theta)/\cos\theta$, and direct substitution into equations (S150)–(S151) shows that $\mathcal{C}_{13} = \mathcal{C}_{23} = 0$, confirming $S_{13} = S_{23} = 0$ as required by the obstruction theorem. These reductions confirm that the two-point theory is fully consistent with the classical one-point framework and demonstrate that the two-point framework is a true generalization rather than an unrelated model, that the unique-ligament energy counting rule is consistent with the original midpoint-cut philosophy, and that the new parameters η, θ_1, and θ_2 enrich the design space without breaking the established theory.

S4. Minimality Theorem: Two-Point Basis as Topological Lower Bound

We now establish a minimality result for the arrangement used in this work. The original version of this document asserted that the two-point basis is the minimal enlargement required to enable shear-normal coupling in planar Y-type hexagonal lattices. That assertion does not survive Proposition S2.8, which exhibits coupling with a single junction type, and it is replaced here by a statement about the alternating arrangement, which is what the argument supports.

Theorem S1 (Minimality of the two-point arrangement)**.** *Within the class of admissible planar Y-type hexagonal lattices:*

1. Balanced uniform lattices are uncoupled*: every uniformly decorated, branch balanced Y-type hexagonal lattice satisfies $S_{13} = S_{23} = 0$, regardless of geometric or material parameters.*
2. Two-point is sufficient*: There exist two-point Y-type hexagonal lattices with $S_{13} \neq 0$ or $S_{23} \neq 0$.*
3. Minimality of the arrangement*: no basis of size smaller than two supports an alternation between two distinct decorations, so $n_{basis} = 2$ is the smallest basis realizing the construction of Section S3.*

Part (iii) concerns this arrangement only. It is not a claim that coupling requires $n_{basis} \geq 2$, which is false by Proposition S2.8.

Proof. Part (i) is Corollary S2.11, whose two hypotheses are uniform decoration and branch balance; by Theorem S7 these give the reflection symmetry $R : (x, y) \mapsto (-x, y)$, and by Theorem S3 that symmetry forces $S_{13} = S_{23} = 0$ for all $(h, L_1, L_2, \theta_1, \theta_2)$ and all (E, ν, t).

Part (ii) follows from the closed forms $S_{13} = \mathcal{C}_{13}/(4E\alpha^3)$ and $S_{23} = \Lambda\mathcal{C}_{23}/(4E\alpha^3 H)$, with $\mathcal{C}_{13}$ and $\mathcal{C}_{23}$ given by (S150) and (S151). At $\eta = 1.2$, $\theta_1 = 30°$, $\theta_2 = -15°$, $\beta = 1$ and $\alpha = 0.05$ these give $\mathcal{C}_{13} = -0.5764$ and $\mathcal{C}_{23} = -0.2883$, both nonzero, and Corollary S3.4

extends this from one point to a set of full measure. Note that the argument runs from the computation to the absence of symmetry, through Corollary S3.5, and not in the opposite direction; the value $\eta = 1.1$ quoted in the original version of this proof has been replaced by $\eta = 1.2$ so that the example agrees with the one used in the main text.

Part (iii) follows from the integrality of the basis size. The construction of Section S3 assigns the two branch families to opposite sides at neighbouring junctions, which requires two distinct junction types within one period. Since n_{basis} is a positive integer there is no admissible value strictly between one and two, and a lattice with $n_{\text{basis}} = 1$ has nothing to alternate between. □

Remark S4.2 (Topological vs. geometric optimization). Theorem S1 has implications for lattice design, although narrower ones than the original version of this remark claimed. Within the balanced and uniformly decorated class, shear-normal coupling is not reachable by geometric fine-tuning: no optimization of lengths (h, L_1, L_2), angles (θ_1, θ_2) or material properties (E, ν, t) can produce it, because the reflection symmetry of the cell forbids it. Leaving that class requires a discrete decision, either to unbalance the branches, which is the slipped lattice of Proposition S2.8, or to enlarge the basis, which is the construction developed here. Once the basis is enlarged to two points, coupling becomes a generic feature controlled by the asymmetry parameters η and (θ_1, θ_2). This separation between topological constraints and geometric degrees of freedom is analogous to the distinction between monatomic and diatomic phononic chains: the former cannot support optical modes regardless of mass or spring constant choices, while the latter can.

Remark S4.3 (Extension to n-point bases). The minimality theorem does not preclude the possibility of using larger bases ($n_{\text{basis}} \geq 3$) to achieve coupling. Indeed, any n-point lattice with $n \geq 2$ that breaks reflection symmetry will generically exhibit nonzero S_{13} and S_{23}. However, such larger bases introduce additional geometric degrees of freedom without fundamentally altering the coupling mechanism. The two-point basis is minimal in the sense that it is the simplest periodic structure capable of coupling, making it the natural starting point for design and the clearest demonstration of the underlying principle.

Remark S4.4 (Comparison with classical metamaterial design). Classical approaches to achieving unusual effective properties in lattice materials typically focus on varying geometric parameters within a fixed unit cell topology. For example, auxetic behavior in re-entrant honeycombs is achieved by varying the angle of inclined members while maintaining a single-cell structure. In contrast, Theorem S1 shows that shear-normal coupling requires a qualitatively different approach: topological enlargement of the basis. This represents a shift from geometric optimization to topological design as the primary mechanism for enabling new constitutive behaviors.

S5. Geometrical and Numerical Results

S5.1. Geometrical Results

The results presented in this subsection illustrate the geometric consequences of the topological transition introduced by the two-point formulation. As established in the preceding sections, enlarging the periodic basis from a single junction to two inequivalent junctions removes the reflection symmetry that enforces $S_{13} = S_{23} = 0$ in the balanced, uniformly decorated case. The lattices shown below are therefore not arbitrary

geometric variations, but explicit realizations of this topological change. By varying the geometric parameters $(L_1, L_2, h, \theta_1, \theta_2)$ within the two-point framework, a wide range of periodic architectures can be generated, including hexagonal, rhombic, rectangular, and auxetic-type morphologies. This diversity arises because the two-point construction permits asymmetric embeddings of the same underlying connectivity, which are inaccessible when all junctions are constrained to be equivalent under translation. The examples presented here demonstrate that the emergence of shear–normal coupling is fundamentally linked to this topological enlargement of the unit-cell basis, and not to any particular choice of geometry.

The lattices shown in Fig. S6 illustrate the range of periodic architectures that can be generated within the proposed two-point framework. In Fig. S6(a), where both inclined ligament families are identical and symmetrically oriented, the structure reduces to a regular hexagonal-type lattice, representing the limiting configuration in which the two-point description collapses to an effectively one-point geometry. Fig. S6(b) demonstrates that, when the vertical ligament is removed, the structure transforms into a dense oblique network composed solely of inclined members, resulting in a strongly direction-dependent topology governed entirely by angular asymmetry. Fig. S6(c) shows that when both inclined families become horizontal, the lattice degenerates into a rectangular grid with aligned horizontal and vertical members, illustrating how the same framework can recover classical orthogonal architectures as a special case. In contrast, Fig. S6(d) produces a highly anisotropic configuration in which one inclined family becomes nearly horizontal and significantly shorter, leading to a stretched and skewed lattice with pronounced directional bias.

The lattices shown in Fig. S7 further illustrate the geometric diversity accessible within the two-point formulation, particularly within configurations that retain a broadly regular structural theme while exhibiting controlled asymmetry. In Fig. S7(a), both inclined ligament families share the same orientation while differing in length, resulting in a regular hexagonal-type lattice with subtle geometric distortion that introduces directional stiffness contrast without breaking the overall cellular structure. Fig. S7(b) demonstrates that introducing angular mismatch between the two families leads to a skewed hexagonal pattern, where the cells become progressively distorted and directional anisotropy becomes more pronounced. In Fig. S7(c), the absence of the vertical ligament combined with a strong disparity in ligament lengths produces a diamond-like network dominated by a single inclined family, illustrating a transition toward a uniaxial structural motif governed primarily by one directional connectivity. Fig. S7(d) represents an intermediate configuration in which one inclined family becomes horizontal while the other remains oblique, giving rise to a hybrid lattice that combines rectangular alignment in one direction with angular connectivity in the other.

The lattices shown in Fig. S8 illustrate configurations within the auxetic design space enabled by the two-point formulation, where opposing ligament orientations give rise to re-entrant geometries and unconventional deformation mechanisms. In Fig. S8(a), the symmetric opposition of the two inclined ligament families produces a classical re-entrant hexagonal morphology, where the inward-pointing cell geometry is expected to promote auxetic deformation through hinging and rotation of the junctions. Fig. S8(b) demonstrates that even when one ligament family is aligned horizontally, the presence of an oppositely inclined family is sufficient to induce a partially re-entrant structure, yielding

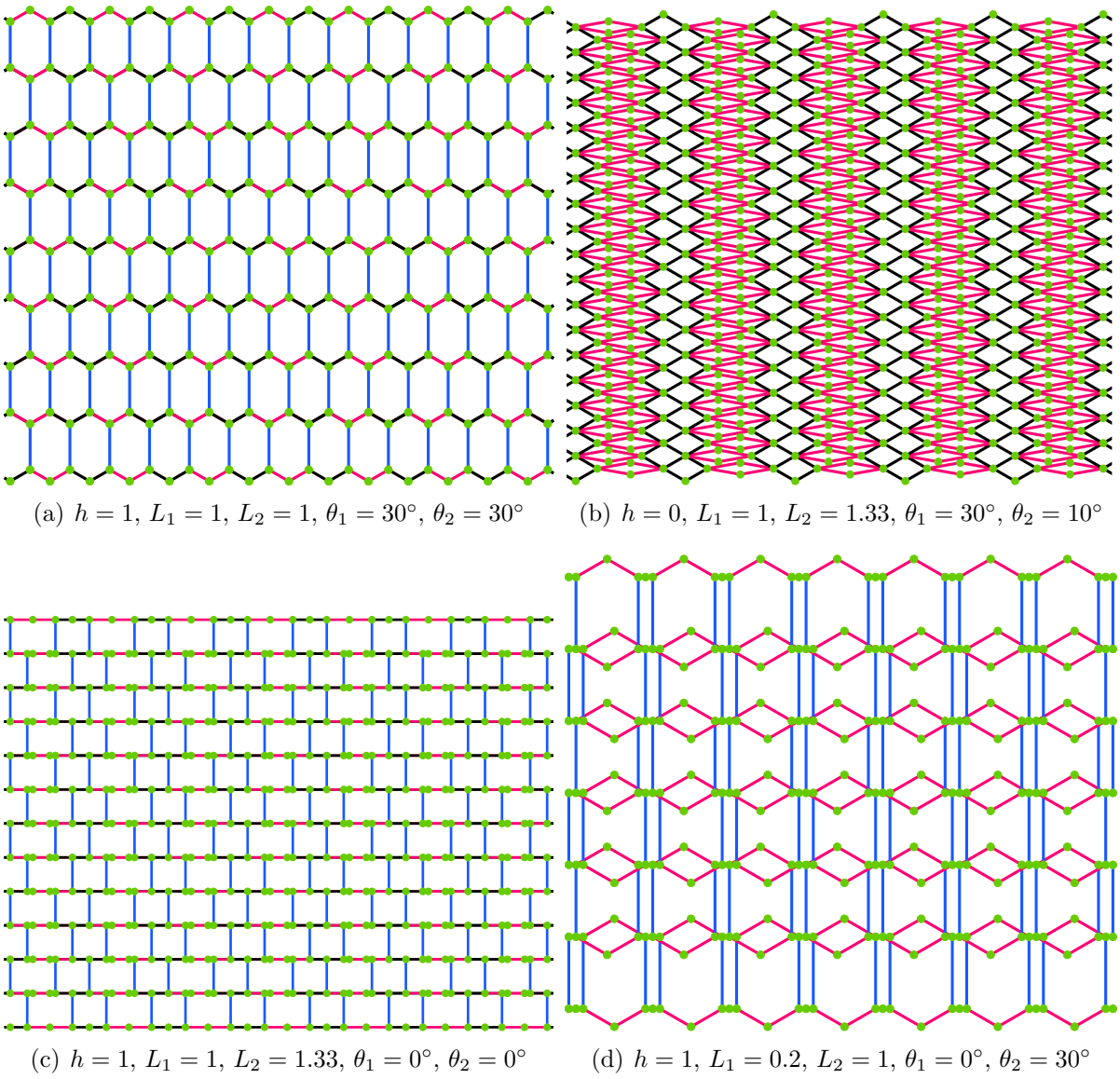

(a) $h = 1$, $L_1 = 1$, $L_2 = 1$, $\theta_1 = 30°$, $\theta_2 = 30°$

(b) $h = 0$, $L_1 = 1$, $L_2 = 1.33$, $\theta_1 = 30°$, $\theta_2 = 10°$

(c) $h = 1$, $L_1 = 1$, $L_2 = 1.33$, $\theta_1 = 0°$, $\theta_2 = 0°$

(d) $h = 1$, $L_1 = 0.2$, $L_2 = 1$, $\theta_1 = 0°$, $\theta_2 = 30°$

Fig. S6. Representative lattice architectures generated by tessellating the two-point unit cell. The four examples illustrate how qualitatively different global patterns emerge from different choices of geometric parameters, ranging from symmetric hexagonal-type arrangements to highly anisotropic and degenerate configurations. These realizations highlight the geometric flexibility enabled by the two-point formulation, in which the two inclined ligament families can independently vary in both orientation and length within a single periodic basis. Such variability is not attainable within the classical one-point framework, where translational symmetry enforces identical junction geometry throughout the lattice.

a hybrid architecture that retains auxetic characteristics while exhibiting directional bias. In Fig. S8(c), increasing both the ligament inclination and vertical separation amplifies the re-entrant effect, resulting in a more open and compliant lattice with enhanced rotational freedom at the junctions. Fig. S8(d) further generalizes this behavior by introducing asymmetric angular pairing, leading to a skewed auxetic topology in which the re-entrant mechanism is directionally non-uniform. Taken together, these examples highlight that auxetic behavior in this framework is not restricted to a single canonical geometry, but emerges as a natural consequence of allowing two independent ligament families with

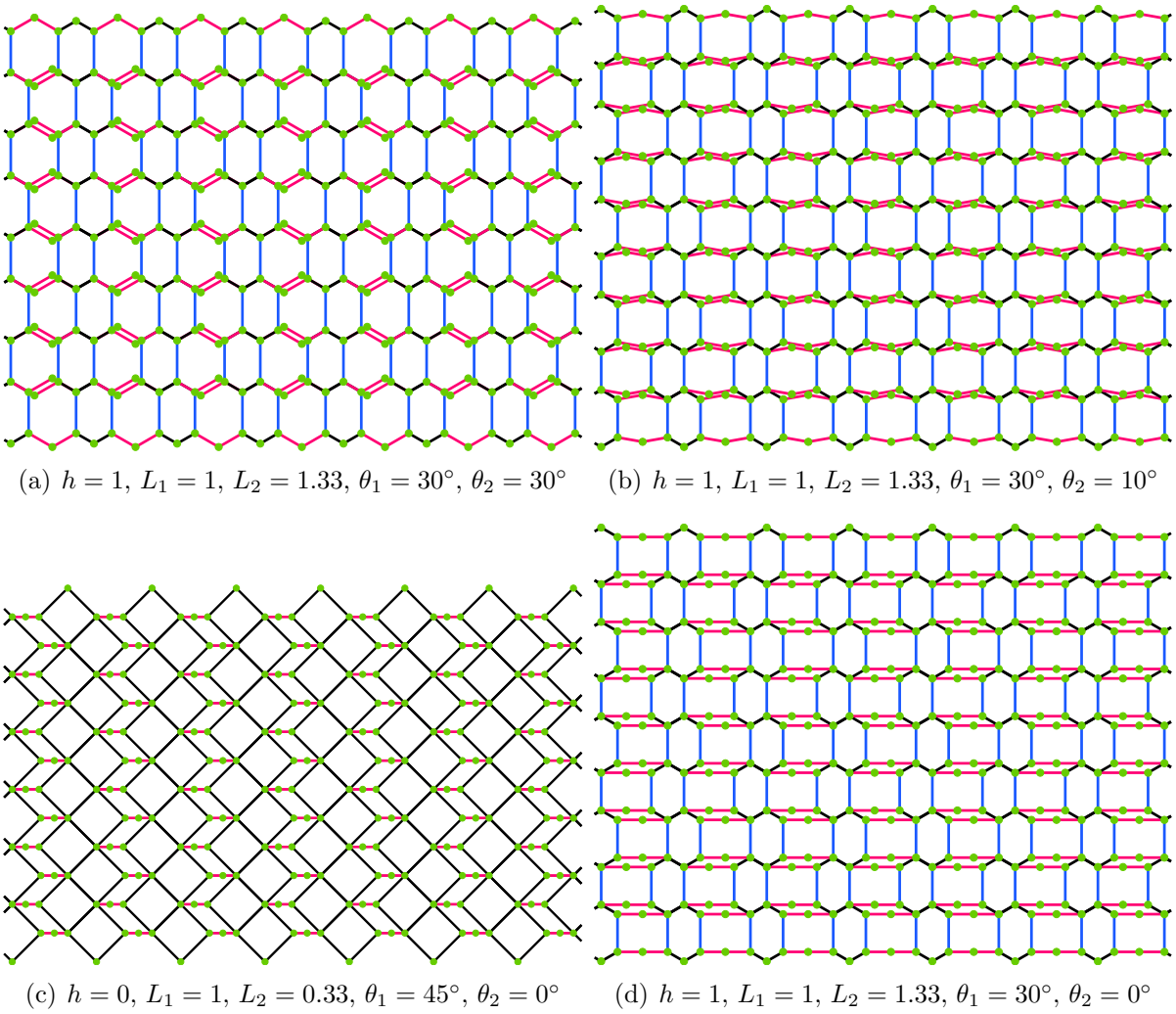

(a) $h = 1$, $L_1 = 1$, $L_2 = 1.33$, $\theta_1 = 30°$, $\theta_2 = 30°$

(b) $h = 1$, $L_1 = 1$, $L_2 = 1.33$, $\theta_1 = 30°$, $\theta_2 = 10°$

(c) $h = 0$, $L_1 = 1$, $L_2 = 0.33$, $\theta_1 = 45°$, $\theta_2 = 0°$

(d) $h = 1$, $L_1 = 1$, $L_2 = 1.33$, $\theta_1 = 30°$, $\theta_2 = 0°$

Fig. S7. Representative lattice architectures within the regular design family generated by the two-point unit cell. These examples demonstrate how variations in ligament length ratios and angular parameters lead to distinct yet structurally coherent periodic patterns. The ability to independently tune the two inclined ligament families enables systematic control over anisotropy and directional stiffness while maintaining global periodicity, a feature not achievable within the classical one-point framework.

opposing orientations. The two-point formulation therefore provides a systematic route to generating and tuning auxetic lattices within a unified periodic setting. In contrast, such re-entrant configurations cannot be realized within the one-point framework, where symmetry enforces identical angular configurations at every junction and precludes the formation of opposing ligament orientations.

It is important to emphasize that, despite the wide diversity of lattice morphologies shown above, all of these configurations are governed by the same analytical framework developed in Section 3. The effective compliance matrix for each lattice can be obtained explicitly from the closed-form expressions for the coefficients S_{ij} in terms of the geometric parameters $(L_1, L_2, h, \theta_1, \theta_2)$. Thus, the two-point formulation not only enables a rich design space at the geometric level, but also provides a unified and fully analytical description of the resulting effective behavior. This establishes a direct and tractable link between lattice topology, geometry, and macroscopic mechanical response.

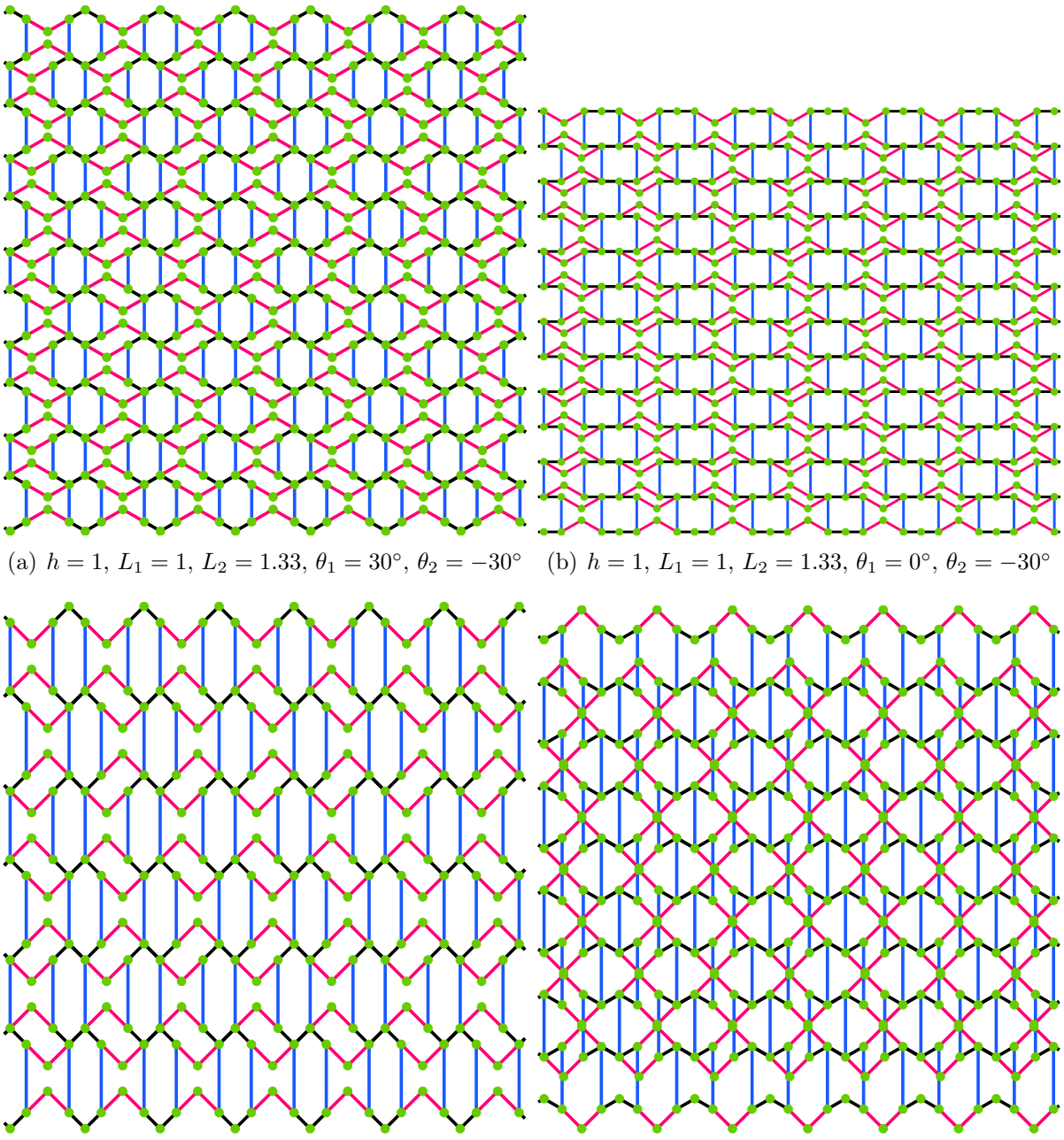

(a) $h = 1$, $L_1 = 1$, $L_2 = 1.33$, $\theta_1 = 30°$, $\theta_2 = -30°$ (b) $h = 1$, $L_1 = 1$, $L_2 = 1.33$, $\theta_1 = 0°$, $\theta_2 = -30°$

(c) $h = 1.5$, $L_1 = 1$, $L_2 = 1.33$, $\theta_1 = 45°$, $\theta_2 = -45°$ (d) $h = 1.5$, $L_1 = 1$, $L_2 = 1.33$, $\theta_1 = -30°$, $\theta_2 = 45°$

Fig. S8. Representative lattice architectures within the auxetic design regime generated by the two-point unit cell. These configurations arise from opposing orientations of the inclined ligament families, producing re-entrant geometries associated with negative Poisson-type responses. The independent control of the two ligament families enables systematic exploration of auxetic behavior within a periodic framework, a feature not attainable in one-point lattices due to inherent symmetry constraints.

S5.2. Numerical Results

The geometric realizations presented in the previous subsection provide explicit examples of the diverse lattice morphologies enabled by the two-point formulation. We now quantify the effective mechanical behaviour associated with these architectures using the analytical expressions derived earlier. In particular, the equivalent stiffnesses, Poisson's

ratios, and coupling coefficients are evaluated as functions of the geometric parameters, with emphasis on the role of the inclination angle θ_2. These numerical results establish a direct connection between the topology-enabled geometric asymmetry of the lattice and its macroscopic response, allowing the influence of different lattice configurations to be systematically interpreted within a unified analytical framework.

The variation of the equivalent Young's moduli with θ_2 in Fig. S9 shows a clear directional asymmetry between the two principal axes. The modulus E_1^{eq} exhibits a pro-

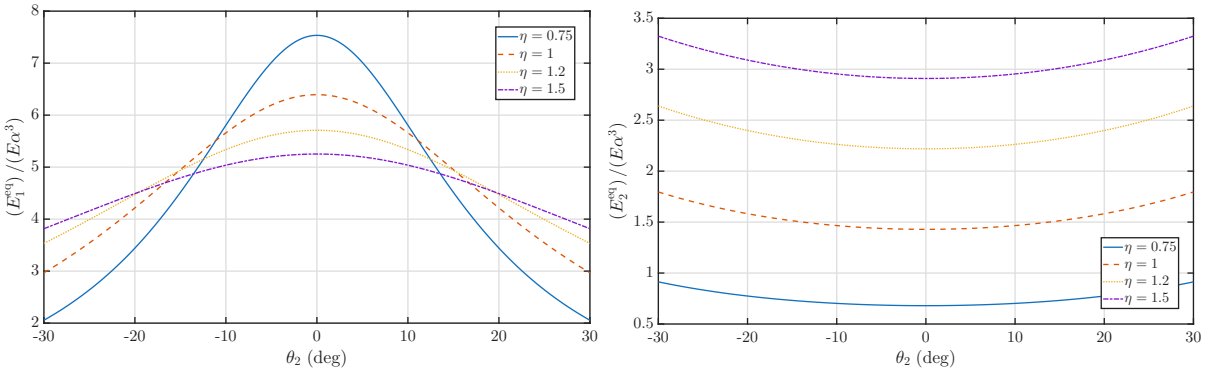

(a) $(E_1^{\text{eq}})/(E\alpha^3)$ (b) $(E_2^{\text{eq}})/(E\alpha^3)$

Fig. S9. Equivalent Young's moduli in the two principal directions as functions of θ_2 for fixed $\theta_1 = 30°$. The results are shown for $\alpha = 0.01$, $\beta = 1/1.5$, and $\eta \in \{0.75, 1, 1.25, 1.5\}$.

nounced peak near $\theta_2 = 0°$, indicating that alignment of the inclined members enhances axial stiffness along direction 1. As $|\theta_2|$ increases, the stiffness decreases due to increasing geometric misalignment and bending-dominated deformation. In contrast, E_2^{eq} displays a shallow minimum near $\theta_2 = 0°$, reflecting a complementary load transfer mechanism in the orthogonal direction. Increasing η systematically raises both moduli, but also reduces sensitivity to θ_2, indicating that geometric asymmetry becomes less influential when the two ligament families are more balanced. Physically, this demonstrates that stiffness anisotropy can be tuned continuously through angular control, with the peak at $\theta_2 = 0°$ corresponding to optimal load alignment.

The equivalent shear modulus shown in Fig. S10 increases monotonically with θ_2 for all values of η, with a convex profile that becomes steeper as η decreases. This indicates that shear resistance is enhanced when the inclined members are oriented away from symmetry, promoting more effective triangulation of the lattice. For small η, the structure is more compliant and thus more sensitive to angular changes, leading to a stronger curvature in the response. For larger η, the response becomes smoother, indicating a more stable shear transfer mechanism. There is no zero crossing or non-monotonic behaviour, which implies that shear stiffness remains strictly positive across the parameter space. Physically, this confirms that the lattice maintains shear stability for all configurations considered, while allowing substantial tunability in magnitude.

The Poisson's ratios in Fig. S11 show rich behaviour, including sign changes that indicate transitions between conventional and auxetic response. The quantity ν_{12}^{eq} exhibits a zero crossing for lower values of η, particularly around $\theta_2 \approx -10°$ for $\eta = 0.75$. On one side of this point, the material behaves conventionally, contracting laterally under axial tension, while on the other side it becomes auxetic, expanding laterally. As η increases, this

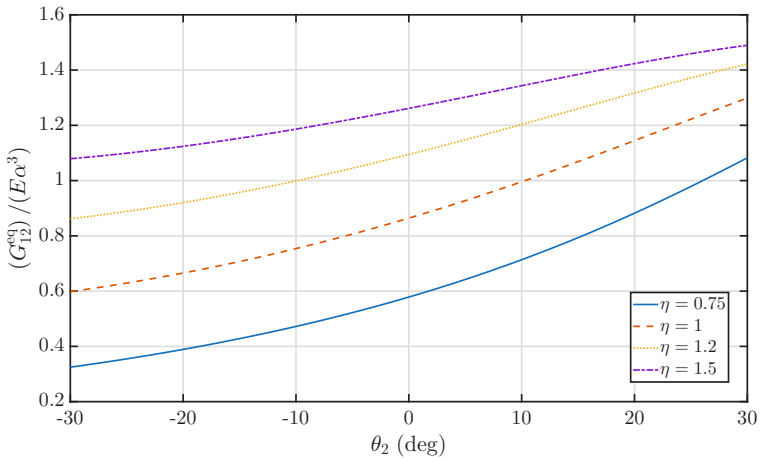

Fig. S10. Equivalent shear modulus as a function of θ_2 for fixed $\theta_1 = 30°$. The results are shown for $\alpha = 0.01$, $\beta = 1/1.5$, and $\eta \in \{0.75, 1, 1.25, 1.5\}$.

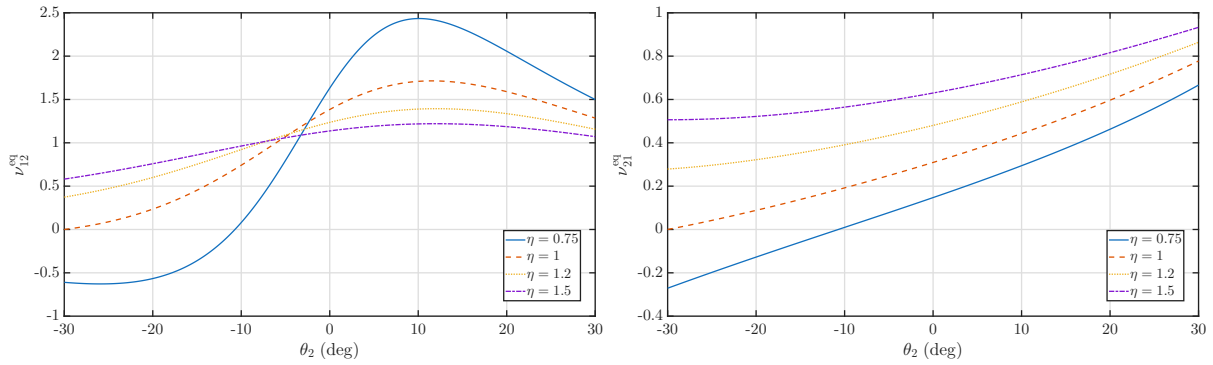

(a) ν_{12}^{eq} (b) ν_{21}^{eq}

Fig. S11. Equivalent Poisson's ratios as functions of θ_2 for fixed $\theta_1 = 30°$. The results are shown for $\alpha = 0.01$, $\beta = 1/1.5$, and $\eta \in \{0.75, 1, 1.25, 1.5\}$.

zero crossing disappears and the response becomes strictly positive, indicating suppression of auxetic behaviour. In contrast, ν_{21}^{eq} increases monotonically with θ_2 and crosses zero for lower η, marking a similar transition but in the orthogonal direction. These zero crossings define boundaries between fundamentally different deformation mechanisms governed purely by geometry within the two-point framework.

The coupling coefficients in Fig. S12 exhibit the most distinctive behaviour, with clear zero crossings and strong dependence on both θ_2 and η. The coefficient S_{13} changes sign near $\theta_2 \approx -5°$ for lower η, indicating a reversal in the coupling between normal strain in direction 1 and shear deformation. On one side of the zero crossing, axial loading induces shear in one sense, while on the other side it induces shear in the opposite sense. Similarly, S_{23} shows a zero crossing at larger θ_2, with a nearly linear variation across the domain for smaller η. The magnitude of both coefficients decreases with increasing η, suggesting that coupling effects are strongest when the two ligament families are highly asymmetric. Physically, these results demonstrate that the two-point lattice can exhibit controllable shear–normal coupling, including complete decoupling at the zero crossings. This behaviour is fundamentally absent in classical one-point lattices, where symmetry

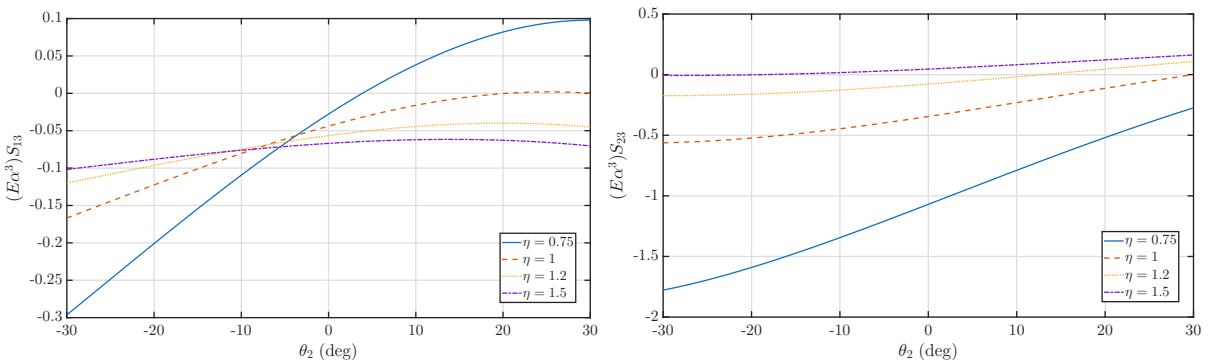

(a) $(E\alpha^3)S_{13}$ (b) $(E\alpha^3)S_{23}$

Fig. S12. Normalized shear–normal coupling coefficients as functions of θ_2 for fixed $\theta_1 = 30°$. The results are shown for $\alpha = 0.01$, $\beta = 1/1.5$, and $\eta \in \{0.75, 1, 1.25, 1.5\}$.

enforces $S_{13} = S_{23} = 0$ identically.

The numerical results presented above demonstrate that the effective mechanical response of the two-point lattice is highly sensitive to geometric asymmetry, with several quantities exhibiting strong nonlinear variation and, in some cases, qualitative transitions such as sign changes. While these full expressions capture the complete behaviour across a wide parameter range, additional insight can be gained by examining the regime of small deviations from the symmetric configuration. In this limit, the governing relations simplify and the emergence of anisotropy and coupling can be understood in a more transparent analytical form. This motivates the asymptotic analysis presented in the following section.

S6. Small Asymmetry Expansion

Having established that two-point lattices generically exhibit nonzero coupling when $\eta \neq 1$ or $\theta_1 \neq \theta_2$, we now analyze the behavior near the symmetric limit through perturbative expansion. This reveals how coupling "turns on" as the system transitions from the symmetric one-point configuration to the asymmetric two-point regime, and provides explicit formulas for designing lattices with weak but controlled coupling.

S6.1. Perturbative Emergence of Coupling

We consider small deviations from the symmetric configuration $\eta = 1$, $\theta_1 = \theta_2 = \theta_0$ by introducing perturbation parameters ϵ and δ such that

$$\eta = 1 + \epsilon, \quad \theta_2 = \theta_1 + \delta, \tag{S161}$$

where $|\epsilon| \ll 1$ and $|\delta| \ll 1$. We fix $\theta_1 = \theta_0$ as the base angle and treat (ϵ, δ) as small parameters controlling the asymmetry.

Theorem S1 (Perturbative emergence of coupling)**.** *Let $\eta = 1 + \epsilon$ and $\theta_2 = \theta_1 + \delta$ with $|\epsilon|, |\delta| \ll 1$. Then the coupling coefficients admit the Taylor expansion*

$$S_{13} = \frac{1}{4E\alpha^3}\left[A_{13}(\theta_1, \beta, \alpha)\epsilon + B_{13}(\theta_1, \beta, \alpha)\delta\right] + O(\epsilon^2, \delta^2, \epsilon\delta), \tag{S162}$$

$$S_{23} = \frac{\cos\theta_1}{2E\alpha^3(\beta + \sin\theta_1)}\left[A_{23}(\theta_1, \beta, \alpha)\epsilon + B_{23}(\theta_1, \beta, \alpha)\delta\right] + O(\epsilon^2, \delta^2, \epsilon\delta), \tag{S163}$$

where the first-order coefficients are the partial derivatives

$$A_{13}(\theta_1,\beta,\alpha)=\left.\frac{\partial \mathcal{C}_{13}}{\partial \eta}\right|_{\eta=1,\theta_2=\theta_1}, \tag{S164}$$

$$B_{13}(\theta_1,\beta,\alpha)=\left.\frac{\partial \mathcal{C}_{13}}{\partial \theta_2}\right|_{\eta=1,\theta_2=\theta_1}, \tag{S165}$$

$$A_{23}(\theta_1,\beta,\alpha)=\left.\frac{\partial \mathcal{C}_{23}}{\partial \eta}\right|_{\eta=1,\theta_2=\theta_1}, \tag{S166}$$

$$B_{23}(\theta_1,\beta,\alpha)=\left.\frac{\partial \mathcal{C}_{23}}{\partial \theta_2}\right|_{\eta=1,\theta_2=\theta_1}, \tag{S167}$$

and they are given in closed form by

$$A_{13}=\alpha^2\left(1+\beta\sin\theta_1\right)-3\beta\sin\theta_1, \tag{S168}$$

$$A_{23}=\frac{\alpha^2\sin\theta_1\left(1+\beta\sin\theta_1\right)+3\beta\cos^2\theta_1}{\cos\theta_1}, \tag{S169}$$

$$B_{13}=\left(1-\alpha^2\right)\left(R_0\cos 2\theta_1-\sin 2\theta_1\right)=\left(1-\alpha^2\right)\frac{\beta\cos 2\theta_1-\sin\theta_1}{\cos\theta_1}, \tag{S170}$$

$$B_{23}=\left(1-\alpha^2\right)\left(1+2\beta\sin\theta_1\right), \tag{S171}$$

where $R_0=(\beta+\sin\theta_1)/\cos\theta_1$ *is the symmetric value of* R*. Three of the four are nonzero throughout the admissible domain;* B_{13} *vanishes on the curve* $\beta=\sin\theta_1/\cos 2\theta_1$*, which passes through the regular honeycomb* $\theta_1=30^\circ$*,* $\beta=1$*.*

Proof. We expand $\mathcal{C}_{13}$ and $\mathcal{C}_{23}$ from (S150) and (S151) about the symmetric point $(\eta,\theta_2)=(1,\theta_1)$. Both vanish there by Theorem S6, so the expansions start at first order and the prefactors Λ/H appearing in S_{23} may be evaluated at the symmetric point, where $\Lambda_0=2\cos\theta_1$ and $H_0=\beta+\sin\theta_1$; the variation of that prefactor multiplies a quantity that vanishes and therefore contributes only at second order. This yields the prefactor $\Lambda_0/(4H_0)=\cos\theta_1/\left[2(\beta+\sin\theta_1)\right]$ displayed in (S163).

Step 1: Expansion of the auxiliary quantities. With $\eta^{-1}=1-\epsilon+O(\epsilon^2)$, $\sin\theta_2=\sin\theta_1+\delta\cos\theta_1+O(\delta^2)$ and $\cos\theta_2=\cos\theta_1-\delta\sin\theta_1+O(\delta^2)$,

$$\Lambda=2\cos\theta_1-\epsilon\cos\theta_1-\delta\sin\theta_1+O(\epsilon^2,\delta^2,\epsilon\delta), \tag{S172}$$

$$H=\beta+\sin\theta_1-\tfrac{1}{2}\epsilon\sin\theta_1+\tfrac{1}{2}\delta\cos\theta_1+O(\epsilon^2,\delta^2,\epsilon\delta), \tag{S173}$$

and therefore, from $R=2H/\Lambda$,

$$R=R_0+\frac{\beta}{2\cos\theta_1}\,\epsilon+\frac{1+\beta\sin\theta_1}{2\cos^2\theta_1}\,\delta+O(\epsilon^2,\delta^2,\epsilon\delta). \tag{S174}$$

The original version of this document asserted that R has no first-order variation, the linear terms having apparently cancelled. That cancellation was an algebraic slip: as (S174) shows, both first-order coefficients are nonzero. The conclusion is nonetheless unaffected, for the reason given in Step 2.

Step 2: The derivative with respect to R *vanishes.* Differentiating (S150) and (S151) with respect to R and then setting $\eta=1$, $\theta_2=\theta_1$,

$$\left.\frac{\partial \mathcal{C}_{13}}{\partial R}\right|_{\text{sym}}=-\sin\theta_1\cos\theta_1+\alpha^2\cos\theta_1\sin\theta_1+\sin\theta_1\cos\theta_1-\alpha^2\cos\theta_1\sin\theta_1=0, \tag{S175}$$

and the same cancellation occurs for $\mathcal{C}_{23}$. The first-order coefficients therefore depend only on the explicit appearances of η and θ_2, and R may be held at R_0 while differentiating. This is why the incorrect expansion of R in the original version did not propagate into A_{13}, and it is the step that was missing there.

Step 3: The four coefficients. Differentiating the explicit η dependence of (S150), through $\eta^{-3} = 1 - 3\epsilon + O(\epsilon^2)$ and $\eta^{-1} = 1 - \epsilon + O(\epsilon^2)$, gives

$$A_{13} = -3\sin\theta_1\,(R_0\cos\theta_1 - \sin\theta_1) + \alpha^2\cos\theta_1\,(\cos\theta_1 + R_0\sin\theta_1)\,, \tag{S176}$$

which reduces to (S168) on substituting R_0. Differentiating the explicit θ_2 dependence gives

$$B_{13} = (R_0\cos 2\theta_1 - \sin 2\theta_1) - \alpha^2\,(R_0\cos 2\theta_1 - \sin 2\theta_1) = \left(1-\alpha^2\right)(R_0\cos 2\theta_1 - \sin 2\theta_1)\,, \tag{S177}$$

which is (S170), since $(\beta+\sin\theta_1)\cos 2\theta_1 - 2\sin\theta_1\cos^2\theta_1 = \beta\cos 2\theta_1 - \sin\theta_1$. The expression given for B_{13} in the original version of this document is not equivalent to this one and is withdrawn. The same two differentiations applied to (S151) give (S169) and (S171).

Step 4: Verification. At $\theta_1 = 30°$, $\beta = 1$ and $\alpha = 0.05$ the closed forms give $A_{13} = -1.4963$, $A_{23} = 2.6002$, $B_{13} = 0$ and $B_{23} = 1.9950$. Numerical differentiation of (S150) and (S151) by central differences reproduces these values to all digits shown, and the vanishing of B_{13} at this geometry is confirmed by direct evaluation, which gives $\mathcal{C}_{13} = -1.50\,\delta^2 + O(\delta^3)$ along $\epsilon = 0$. A second check at $\theta_1 = 47°$, $\beta = 0.7$ gives $B_{13} = -1.1411$ from either form of (S170).

Step 5: Generic nonvanishing. The numerator of A_{23} in (S169) is dominated by $3\beta\cos^2\theta_1$ throughout the slender range and is therefore positive, so $A_{23} \neq 0$ on the admissible domain and coupling is first order in the length asymmetry everywhere. The angular sensitivities B_{13} and B_{23} carry the common factor $1-\alpha^2$, which is positive for admissible slenderness, and $B_{23} > 0$ for $\theta_1 > 0$; only B_{13} can vanish, and it does so exactly on the curve $\beta = \sin\theta_1/\cos 2\theta_1$. □

Remark S6.2 (Linear emergence and phase transition analogy). Theorem S1 shows that coupling emerges *linearly* with asymmetry, not quadratically, with the single exception of the response of S_{13} to angular asymmetry on the curve $\beta = \sin\theta_1/\cos 2\theta_1$, where B_{13} vanishes and the response is quadratic. This is analogous to a continuous phase transition in statistical mechanics, where an order parameter (here, the coupling coefficients) grows linearly from zero as a control parameter (here, ϵ or δ) crosses a critical value (here, zero). The symmetric configuration $\eta = 1, \theta_1 = \theta_2$ acts as a critical point separating the zero-coupling phase (one-point effective behavior) from the nonzero-coupling phase (genuine two-point behavior). The linear scaling implies that even small asymmetries produce measurable coupling, making the effect experimentally accessible.

S6.2. Zero Crossings and Sign Changes

The coupling coefficients S_{13} and S_{23} are not merely nonzero away from the symmetric limit, they can also change sign depending on the asymmetry parameters. These zero crossings have important physical implications for the directional sense of coupling and for tailoring constitutive responses.

Proposition S6.3 (Existence of zero crossings)**.** *For fixed values of* $(\beta, \alpha, \theta_1)$*, there exist curves in the* (ϵ, δ) *parameter space along which* $S_{13} = 0$ *or* $S_{23} = 0$ *individually, and these curves generically pass through the origin* $(\epsilon, \delta) = (0, 0)$*.*

Proof. From Theorem S1, the condition $S_{13} = 0$ to first order requires

$$A_{13}\epsilon + B_{13}\delta = 0 \quad \Rightarrow \quad \delta = -\frac{A_{13}}{B_{13}}\epsilon, \tag{S178}$$

provided $B_{13} \neq 0$. This defines a straight line through the origin in the (ϵ, δ) plane. Similarly, $S_{23} = 0$ defines another line

$$\delta = -\frac{A_{23}}{B_{23}}\epsilon. \tag{S179}$$

These two lines generically have different slopes (since the ratios A_{13}/B_{13} and A_{23}/B_{23} differ), dividing the (ϵ, δ) plane into four quadrants with different sign combinations for (S_{13}, S_{23}). The origin $(\epsilon, \delta) = (0, 0)$ is the unique point where both coupling coefficients vanish simultaneously. □

Definition S6.4 (Sign quadrants)**.** The (ϵ, δ) parameter plane near the origin is divided into four regions based on the signs of S_{13} and S_{23}:

$$\text{Quadrant I:} \quad S_{13} > 0,\ S_{23} > 0, \tag{S180}$$

$$\text{Quadrant II:} \quad S_{13} < 0,\ S_{23} > 0, \tag{S181}$$

$$\text{Quadrant III:} \quad S_{13} < 0,\ S_{23} < 0, \tag{S182}$$

$$\text{Quadrant IV:} \quad S_{13} > 0,\ S_{23} < 0. \tag{S183}$$

The physical interpretation of these sign changes is as follows. Recall that S_{13} relates shear stress τ_{12} to normal strain ε_{11} via $\varepsilon_{11} = S_{13}\tau_{12}$, and S_{23} relates shear stress to normal strain ε_{22} via $\varepsilon_{22} = S_{23}\tau_{12}$. When $S_{13} > 0$, a positive shear stress (tending to shear the lattice in the positive 1-2 direction) induces tensile normal strain in the 1-direction, meaning the lattice elongates horizontally under shear. Conversely, when $S_{13} < 0$, the same shear stress induces compressive normal strain, meaning the lattice contracts horizontally. Similarly, the sign of S_{23} controls whether the lattice elongates or contracts vertically under shear. The four quadrants therefore correspond to four qualitatively different coupling behaviors:

- *Quadrant I* $(S_{13} > 0, S_{23} > 0)$: Positive shear induces biaxial tension (expansion in both directions).
- *Quadrant II* $(S_{13} < 0, S_{23} > 0)$: Positive shear induces horizontal compression and vertical tension.
- *Quadrant III* $(S_{13} < 0, S_{23} < 0)$: Positive shear induces biaxial compression (contraction in both directions).
- *Quadrant IV* $(S_{13} > 0, S_{23} < 0)$: Positive shear induces horizontal tension and vertical compression.

The ability to tune the signs of S_{13} and S_{23} independently by adjusting (ϵ, δ) provides a powerful design tool. For applications requiring specific directional responses to shear, such as deployable structures, morphing skins, or vibration control devices, the sign quadrants offer distinct operational modes that can be accessed by geometric tailoring of the two-point lattice.

Remark S6.5 (Design implications). The zero-crossing structure revealed by Proposition S6.3 has practical design implications. If a target application requires, say, $S_{13} > 0$ with $S_{23} \approx 0$ (horizontal elongation under shear with minimal vertical coupling), one can choose (ϵ, δ) near the zero line of S_{23} but away from the zero line of S_{13}. Conversely, if one desires strong coupling in both directions with a specific ratio $S_{13}/S_{23} = c$, one selects parameters along the ray satisfying $(A_{13}\epsilon + B_{13}\delta)/(A_{23}\epsilon + B_{23}\delta) = c$. The perturbative formulas (S162)–(S163) thus provide an explicit roadmap for inverse design: given target coupling values, solve for the required asymmetry parameters.

Remark S6.6 (Higher-order corrections). The expansions (S162)–(S163) are valid for small $|\epsilon|, |\delta| \ll 1$. For moderate asymmetries, second-order corrections of the form $C_{ij}\epsilon^2 + D_{ij}\delta^2 + E_{ij}\epsilon\delta$ become important and can modify the locations of zero crossings away from the linear predictions. Nevertheless, the qualitative structure, existence of zero lines dividing sign quadrants, persists at higher orders, with the lines becoming curves. For large asymmetries ($|\epsilon|$ or $|\delta|$ of order unity), the full nonlinear expressions (S150)–(S151) must be used, as discussed in the parametric analysis of Section 5.

S6.3. Exact zero crossings of S_{13} and S_{23}

We now derive the exact, fully nonlinear zero-crossing conditions for the shear-normal coupling coefficients S_{13} and S_{23}, without invoking the perturbative expansion.

Let

$$s_1 = \sin\theta_1, \qquad c_1 = \cos\theta_1, \qquad s_2 = \sin\theta_2, \qquad c_2 = \cos\theta_2, \tag{S184}$$

and define

$$\Lambda = c_1 + \eta^{-1}c_2, \qquad H = \beta + \frac{1}{2}\left(s_1 + \eta^{-1}s_2\right), \tag{S185}$$

together with

$$T = (1-\alpha^2)s_1c_1 + (\eta^{-3} - \alpha^2\eta^{-1})s_2c_2. \tag{S186}$$

S6.3.1. Zero crossing of S_{13}

From the exact constitutive expressions, the shear-normal coupling coefficient can be written as

$$S_{13} = \frac{1}{2E\alpha^3}\frac{T}{\Lambda}. \tag{S187}$$

Hence the exact condition for $S_{13} = 0$ is equivalent, for admissible geometries with $\Lambda \neq 0$, to $T = 0$:

$$(1-\alpha^2)\sin\theta_1\cos\theta_1 + (\eta^{-3} - \alpha^2\eta^{-1})\sin\theta_2\cos\theta_2 = 0. \tag{S188}$$

Equivalently,

$$(1-\alpha^2)\sin 2\theta_1 + (\eta^{-3} - \alpha^2\eta^{-1})\sin 2\theta_2 = 0. \tag{S189}$$

Therefore,

$$\sin 2\theta_2 = -\frac{1-\alpha^2}{\eta^{-3} - \alpha^2\eta^{-1}}\sin 2\theta_1 = -\frac{\eta^3(1-\alpha^2)}{1-\alpha^2\eta^2}\sin 2\theta_1. \tag{S190}$$

Whenever the right-hand side lies in $[-1, 1]$, the zero-crossing angles are given by

$$2\theta_2 = \sin^{-1}\left(-\frac{\eta^3(1-\alpha^2)}{1-\alpha^2\eta^2}\sin 2\theta_1\right) + 2\pi k, \tag{S191}$$

or

$$2\theta_2 = \pi - \sin^{-1}\left(-\frac{\eta^3(1-\alpha^2)}{1-\alpha^2\eta^2}\sin 2\theta_1\right) + 2\pi k, \qquad k \in \mathbb{Z}. \tag{S192}$$

S6.3.2. Zero crossing of S_{23}

From the exact formula

$$S_{23} = \frac{\Lambda}{4E\alpha^3 H}\,\mathcal{C}_{23}, \qquad \Lambda = \cos\theta_1 + \eta^{-1}\cos\theta_2, \qquad H = \beta + \frac{1}{2}\left(\sin\theta_1 + \eta^{-1}\sin\theta_2\right), \tag{S193}$$

the condition $S_{23} = 0$ is equivalent, for admissible geometries with $\Lambda \neq 0$ and $H \neq 0$, to $\mathcal{C}_{23} = 0$.

Introducing

$$p = 1 - \alpha^2, \qquad q = \eta^{-3} - \alpha^2\eta^{-1}, \tag{S194}$$

the exact zero-crossing condition reduces to

$$\begin{aligned}\left(2\beta + \sin\theta_1 + \eta^{-1}\sin\theta_2\right)\left[\left(1 + \alpha^2 - \eta^{-3} - \alpha^2\eta^{-1}\right) + p\cos 2\theta_1 - q\cos 2\theta_2\right] \\ = \left(\cos\theta_1 + \eta^{-1}\cos\theta_2\right)\left(p\sin 2\theta_1 - q\sin 2\theta_2\right).\end{aligned} \tag{S195}$$

This equation defines the exact nonlinear zero-crossing curve of S_{23} in parameter space. In contrast to the case of S_{13}, it does not generally admit an explicit closed-form solution for θ_2, but (S195) is already a substantial simplification of the original expression and is convenient for both analysis and numerical evaluation.

Equation (S189) shows that the sign change of S_{13} is governed by a balance between the contributions of the two inclined ligament families to the shear-normal coupling. On one side of the zero-crossing curve, $S_{13} < 0$, corresponding to shear stress inducing compressive normal strain in the 1-direction, whereas on the other side $S_{13} > 0$, corresponding to shear stress inducing tensile normal strain. Similarly, (S195) defines the exact locus at which the normal strain in the 2-direction induced by shear changes sign. Thus, the zero-crossing curves separate regions with qualitatively different coupling mechanisms and provide exact design boundaries in the (η, θ_2) plane.

The contour plots in Fig. S13 provide a direct geometric interpretation of the coupling mechanisms encoded in S_{13} and S_{23}. The zero-contour lines mark critical boundaries in the (η, θ_2) parameter space where the corresponding coupling terms change sign, separating regimes with qualitatively different deformation responses. On either side of these curves, the coupling between axial and transverse deformation switches orientation, indicating a transition in the internal load-transfer pathways of the lattice. Notably, the smooth and continuous nature of these zero loci suggests that these transitions are not associated with singular behaviour, but rather emerge from gradual geometric reconfiguration of the unit cell. The distinct curvature and positioning of the $S_{13} = 0$ and $S_{23} = 0$ contours further reveal that these two coupling terms are governed by different geometric sensitivities, highlighting their independent roles in controlling anisotropy and directional stiffness. As such, these maps serve as design diagrams, enabling precise identification of parameter regimes where specific coupling effects can be activated, suppressed, or reversed.

Slender limit ($\alpha^2 = 0$). In the slender-beam limit $\alpha^2 \to 0$, the zero-crossing conditions simplify considerably and admit compact closed forms. In this limit,

$$p = 1, \qquad q = \eta^{-3}, \tag{S196}$$

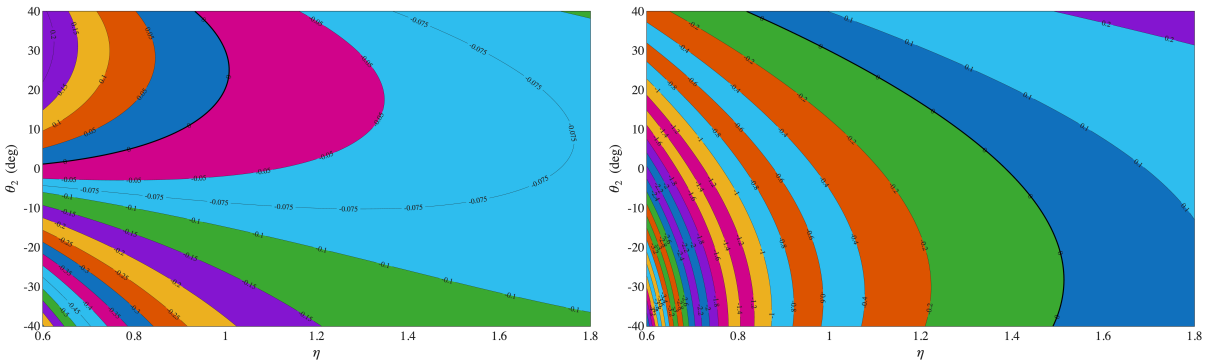

(a) $\alpha^3 S_{13}$ with zero contour (b) $\alpha^3 S_{23}$ with zero contour

Fig. S13. Contour maps of the scaled coupling coefficients $\alpha^3 S_{13}$ and $\alpha^3 S_{23}$ in the (η, θ_2) parameter space for fixed $\theta_1 = 30°$. The black curves denote the exact zero-contour loci, which separate regions of opposite coupling sign. These boundaries define transitions in the effective mechanical response, where the associated coupling term changes from tensile-dominated to compressive-dominated behaviour. The smooth variation of the contours indicates that the sign change is governed by global geometric interactions rather than local instabilities. The distinct shapes of the zero-contours for S_{13} and S_{23} highlight the fundamentally different roles of these coupling terms in controlling anisotropic deformation mechanisms.

so that the condition $S_{13} = 0$ reduces to

$$\sin 2\theta_1 + \eta^{-3} \sin 2\theta_2 = 0, \tag{S197}$$

or equivalently,

$$\sin 2\theta_2 = -\eta^3 \sin 2\theta_1. \tag{S198}$$

Thus, the zero crossing of S_{13} is governed purely by a trigonometric balance between the two inclined ligament families, weighted by the cubic length ratio η^3.

For S_{23}, the exact condition (S195) simplifies to

$$\left(2\beta + \sin\theta_1 + \eta^{-1} \sin\theta_2\right) \left[(1 - \eta^{-3}) + \cos 2\theta_1 - \eta^{-3} \cos 2\theta_2\right] = \left(\cos\theta_1 + \eta^{-1} \cos\theta_2\right) \left(\sin 2\theta_1 - \eta^{-3} \sin 2\theta_2\right). \tag{S199}$$

These expressions reveal a clear separation of roles. The condition for $S_{13} = 0$ depends only on the relative angular configuration of the two ligament families and is independent of the vertical offset parameter β. In contrast, the zero crossing of S_{23} retains an explicit dependence on β through the factor $(2\beta + \sin\theta_1 + \eta^{-1} \sin\theta_2)$, indicating that the two shear-normal coupling coefficients are controlled by different geometric mechanisms. The coefficient S_{13} is governed purely by angular asymmetry between ligament families, whereas S_{23} additionally depends on the vertical positioning of the nodes. Consequently, even in the slender limit, S_{13} and S_{23} respond differently to geometric perturbations, reflecting their distinct coupling structures.

S7. Conclusion

This supplementary document provides the complete mathematical foundations for the symmetry breaking and emergent shear-normal coupling results presented in the main text. We have established four principal contributions: the mirror criterion for the vanish-

ing of shear-normal coupling, with its two hypotheses of uniform decoration and branch balance stated explicitly and shown to be independent; a minimality result for the alternating two-point arrangement; closed-form analytical expressions for all compliance coefficients derived through energy-based homogenization; and a perturbative analysis of the near-symmetric regime including the four first-order sensitivities in closed form.

Section S2 develops the obstruction theory in corrected form. Theorem S7 proves that a uniformly decorated Y-type hexagonal lattice possesses the reflection symmetry $R : (x, y) \mapsto (-x, y)$ if and only if its junctions are branch balanced, $a_L + a_R = 0$ and $b_L = b_R$, and Theorem S3 shows that this symmetry enforces $S_{13} = S_{23} = 0$. Section S2.3 establishes that balance is not a consequence of periodicity: the boundary of a hexagonal cell of this class contains two stems and four branches, its closure identity (S53) holds for every choice of branch projections, and Proposition S2.8 builds from this an admissible lattice with a single junction type and generically nonzero coupling. The closure argument of the original version, which asserted a cell bounded by six inclined members and derived $a_L + a_R = 0$ from it, is therefore withdrawn. Theorem S1 states the minimality that survives, namely that two is the smallest basis supporting the alternating arrangement studied here. Section S3 derives the complete elastic response for two-point lattices using energy-based homogenization. Rather than numerical methods, we obtain closed-form expressions for all compliance coefficients in terms of the geometric parameters $(h, L_1, L_2, \theta_1, \theta_2)$ and dimensionless groups (η, α, β). This systematic framework reveals how breaking reflection symmetry enables non-reciprocal deformation modes coupling extension and shear.

Section S5 evaluates the closed-form expressions numerically across the design space. Figures S9–S12 show that two-point lattices access a wide range of Poisson ratios while maintaining positive definite elasticity tensors. The coupling coefficients S_{13} and S_{23} exhibit zero crossings and sign changes as functions of inclination angle, consistent with their geometric origin rather than material dependence. The internal consistency of the closed forms is checked against Maxwell reciprocity, which holds identically, and against the symmetric limit, at which both coupling coefficients vanish exactly. The sentence claiming an independent finite-element homogenization has been removed: no such computation is reported in the main text or here, and the claim was incorrect. Section S6 develops a perturbative expansion showing coupling emerges linearly from the symmetric limit: $S_{13}, S_{23} \sim \mathcal{O}(\epsilon)$ where ϵ parameterizes deviation from symmetry. This reveals the dual character of the transition: discrete in the decoration of the basis, which is either uniform or not, but continuous at the constitutive level, since the coupling magnitude scales smoothly with the asymmetry. Together with the main paper, this work establishes the mirror content of the unit cell as the primary determinant of which constitutive couplings are accessible in periodic lattice metamaterials. Two geometric ingredients build that mirror, the balance of the two branches at a junction and the uniformity of the decoration across the basis, and each can be removed independently; the two-point construction removes the second and is the case for which the complete closed-form compliance is obtained.